Smart Materials and Structures

On-demand contactless programming of nonlinear elastic moduli in hard magnetic soft beam based broadband active lattice materials

To cite this article: P Sinha and T Mukhopadhyay 2023 *Smart Mater. Struct.* **32** 055021

OPEN ACCESS
IOP Publishing
Smart Materials and Structures
Smart Mater. Struct. 32 (2023) 055021 (24pp)
https://doi.org/10.1088/1361-665X/acc43b

On-demand contactless programming of nonlinear elastic moduli in hard magnetic soft beam based broadband active lattice materials

P Sinha[1] **and T Mukhopadhyay**[2,*]

[1] Department of Aerospace Engineering, Indian Institute of Technology Kanpur, Kanpur, India
[2] School of Engineering, University of Southampton, Southampton, United Kingdom

E-mail: t.mukhopadhyay@soton.ac.uk

Received 18 January 2023, revised 10 March 2023
Accepted for publication 14 March 2023
Published 13 April 2023

Abstract

Engineered honeycomb lattice materials with high specific strength and stiffness along with the advantage of programmable direction-dependent mechanical tailorability are being increasingly adopted for various advanced multifunctional applications. To use these artificial microstructures with unprecedented mechanical properties in the design of different application-specific structures, it is essential to investigate the effective elastic moduli and their dependence on the microstructural geometry and the physics of deformation at the elementary level. While it is possible to have a wide range of effective mechanical properties based on their designed microstructural geometry, most of the recent advancements in this field lead to passive mechanical properties, meaning it is not possible to actively modulate the lattice-level properties after they are manufactured. Thus the on-demand control of mechanical properties is lacking, which is crucial for a range of multi-functional applications in advanced structural systems. To address this issue, we propose a new class of lattice materials wherein the beam-level multi-physical deformation behavior can be exploited as a function of external stimuli like magnetic field by considering hard magnetic soft beams. More interestingly, effective property modulation at the lattice level would be contactless without the necessity of having a complex network of electrical circuits embedded within the microstructure. We have developed a semi-analytical model for the nonlinear effective elastic properties of such programmable lattice materials under large deformation, wherein the mechanical properties can be modulated in an expanded design space of microstructural geometry and magnetic field. The numerical results show that the effective properties can be actively modulated as a function of the magnetic field covering a wide range (including programmable state transition with on-demand positive and negative values), leading to the behavior of soft polymer to stiff metals in a single lattice microstructure according to operational demands.

---

[*] Author to whom any correspondence should be addressed.

1361-665X/23/055021+24$33.00 Printed in the UK

Supplementary material for this article is available online

Keywords: active lattice materials, hard magnetic soft beams, nonlinear in-plane elastic moduli, on-demand property modulation, contactless stiffness control; programmable stiffness

(Some figures may appear in colour only in the online journal)

---

1. Introduction

Metamaterials are a class of materials with properties that are not found or are rare in naturally-occurring materials. By engineering them at the micro-level, we can achieve desired properties like high specific stiffness or strength at the macro level. In such materials, the effective properties are characterized by their structural configuration and not by their intrinsic material properties alone. We can modulate the global mechanical properties of mechanical metamaterials by controlling their microstructural geometric parameters, which can be tuned to present unprecedented novel characteristics like negative elastic moduli, auxetic characteristics, extreme multi-physical properties, meta-fluid properties, high crushing resistance, shock absorption characteristics, negative mass density, etc [1–12]. Lattice-based materials are a class of metamaterials that have a typical feature of unit cell periodicity [13–17]. The geometric characteristics of the periodic unit cell determine the overall mechanical properties of these lattice-based metamaterials [15, 18]. Such materials can meet various application-specific requirements owing to their multi-physical properties that range over varying length scales (nano to macro). These engineered materials have drawn the attention of the scientific community significantly in the recent past, especially owing to the advancements in additive manufacturing techniques. Metamaterials, when compared to conventional composites, provide a larger design input parameter space for property modulation, and while achieving more extreme and multifunctional properties [19–23].

Lattice-based materials, being light and able to exhibit high stiffness, are used in several lightweight systems like sandwich structures [24–29]. Further, the lattice-type structural configurations are found in plenty across different length scales (including nano and micro) of naturally occurring matters [30–34]. Recent trends in engineered materials try to propose intuitive microstructural configurations in a forward framework, or designs identified through computer simulations such as topology optimization. Anisotropy tailoring for lattices made up of multiple materials is presented in [35], where their differing properties are utilized to enhance the design space beyond the geometry of microstructure only. The voltage-dependent Young's moduli of piezo-electric lattice-based microstructures are shown recently to have values that vary from positive to negative [36]. The randomness and disorder in geometric parameters considering the irregularities in manufacturing are studied by considering voronoi honeycombs and through quasi-random configurations [33, 37–41]. The effect of intrinsic stresses in honeycomb lattices is characterized in a recent study [42]. Besides a wide range of investigations concerning 2D lattices, multiple analyses of 3D microstructures and cellular foams have recently been reported [43–46]. On careful examination of the above presented brief literature review, we find that for periodic lattice structures, in general, a unit cell-based approach is considered to analyze the effective mechanical properties [15].

While it is possible to have a wide range of effective mechanical properties based on their designed microstructural geometry, most of the recent advancements in this field lead to passive mechanical properties, meaning it is not possible to actively modulate the lattice-level properties after they are manufactured. Thus the on-demand control of mechanical properties is lacking, which is crucial for a range of multi-functional applications in advanced structural systems. To address this issue, we propose a new class of lattice materials wherein the beam-level multi-physical deformation behavior can be exploited as a function of external stimuli like magnetic field by considering hard magnetic soft (HMS) beams [47, 48]. Since the effective properties of lattices (such as deformation under different loading conditions, vibration, wave propagation, buckling, etc) are essentially derived from the beam-level deformation mechanics, it is possible to control such effective lattice-level properties actively by the intensity and direction of magnetic field. More interestingly, effective property modulation at the lattice level would be contactless without the necessity of having a complex network of electrical circuits embedded within the microstructure [49, 50]. The focus of this work is to investigate the effective nonlinear elastic properties of HMS beam lattice materials, which is essential to analyze these active lattices for static, dynamic and instability characteristics.

HMS materials are a novel class of smart materials that are obtained by embedding particles of hard magnetic materials into soft materials [47, 48]. These are named so because they are soft mechanically, yet hard magnetically. Here the residual magnetic flux is reoriented using an external magnetic field. By hard magnetic, it is implied that high-coercivity ferromagnetic materials are embedded in soft materials [51–53]. This high coercivity helps them retain high magnetic flux density. HMS beams can undergo complex large deformations under various magnetic actuations. These HMS structures can be printed using additive manufacturing techniques by using the magnetic actuation field. Different motion shapes of HMS structures can be realized by varying the magnetic field, opening the design space in soft robotics, biomedical

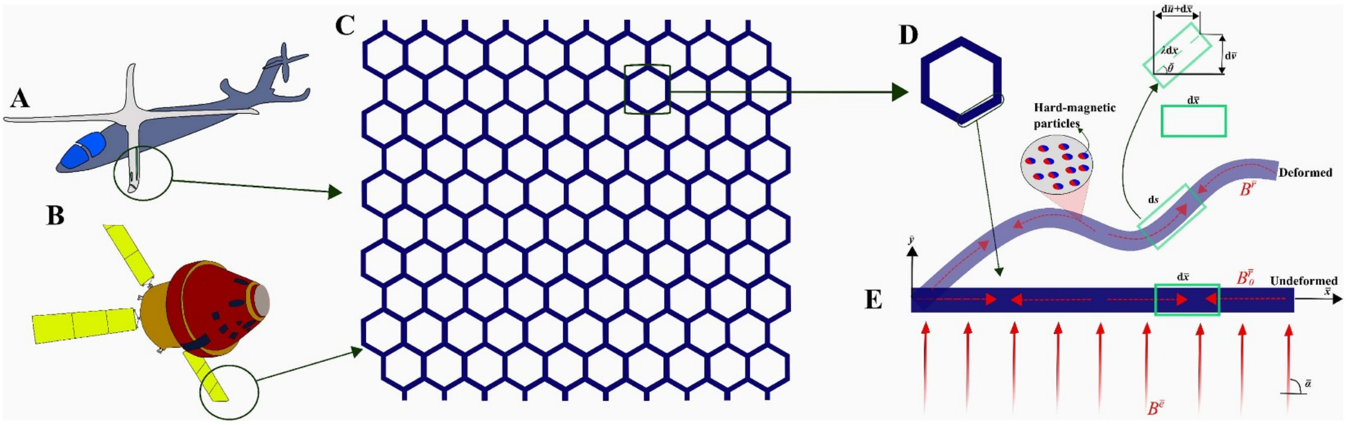

Figure 1. Contactless on-demand modulation of elastic properties in HMS lattice materials. (A) and (B) Typical examples of prospective lattice-based structures where intelligent design of microstructural geometry can lead to unprecedented active mechanical properties at macro-scale. (C) A 2D regular honeycomb lattice. (D) A honeycomb unit cell representing the whole 2D lattice structure. (E) HMS beam-like element representing a cell wall of the unit cell. A HMS beam in both undeformed and deformed configurations under external magnetic actuation is shown, which includes the coordinate system and geometrical relationship of the beam element. The entire lattice is formed by a periodic repetition of the unit cells which are formed through a network of HMS beams. Here, we follow an incremental load step method for analyzing the effective elastic constants of lattice materials. The effect of magnetic actuation is considered in the deformation characteristics of the elementary beams at the local level, considering both bending and axial deformations. Subsequently, this multi-physical effect is propagated to the lattice level through analyzing the mechanics of a unit cell in a bottom-up semi-analytical framework.

devices and flexible electronics [53]. In this article, we conceptualize a lattice network of such HMS beams under the combined influence of magnetic field and mechanical loads, where broadband stiffness modulation can be realized at the global level. It would permit active modulation of elastic properties of the honeycomb lattice (leading to a seamless on-demand conversion of hard and soft material under normal and shear modes of deformation) by intelligently using the desired residual magnetic flux density, keeping the material properties, geometry of microstructure and lattice density unaltered. For doing so, it is imperative that we have an efficient model which could determine the effective elastic constants of lattice materials in terms of the applied magnetic field and far-field mechanical forces along with geometry the of microstructure and intrinsic material properties under normal and shear modes of lattice-level deformations. Further, nonlinear large deformation analyses concerning effective elastic properties of lattice metamaterials are scarce to find in the literature.

In this article, we aim to develop a semi-analytical model for the nonlinear effective elastic properties of programmable lattice materials under large deformation, wherein the mechanical properties can be modulated in an expanded design space of microstructural geometry and magnetic field. We will first develop a numerical model to obtain the nonlinear large deflection profile of HMS beams under a combined magnetic field and mechanical load. The compound mechanics of elementary beam-level transverse and bending deflections would in turn be exploited in a semi-analytical unit cell based framework to evaluate the effective elastic moduli of honeycomb lattice materials (refer to figure 1). Thus we integrate the beam-level multi-physical deformation mechanics and the lattice geometry to have an expanded design space of active and passive parameters. In this work, our focus is essentially on hexagonal lattice materials (refer to figure 1(C)) for demonstrating the concept of contactless active modulation. While such hexagonal lattices are directly relevant to obtaining results for auxetic and non-auxetic configurations along with other lattices like rhombic and rectangular forms, the proposed approach of contactless active modulation through HMS beam networks is generic and it can be extended to a wide range of two and three-dimensional lattices by considering appropriate unit cells. Hereafter, this paper is structured as, section 2: the numerical model for the analysis of HMS beams under combined magnetic field and mechanical load, followed by the development of a lattice-level semi-analytical framework for the nonlinear elastic moduli of metamaterials, section 3: numerical results concerning contactless active modulation of the elastic moduli along with adequate validation at the beam and lattice levels, section 4: conclusions and perspective of the current research.

2. Nonlinear mechanics of HMS beam lattices

In this section, we would first present the beam-level mechanics of HMS beams, followed by a unit cell-based analysis for evaluating lattice-level effective properties. To understand the mechanics of HMS structures, it is necessary to theoretically model them. However, the modeling of HMS structures is a challenge due to the geometric and material nonlinearities. The geometric nonlinearity arises due to large deformation, while the magneto-elastic coupling gives rise to material nonlinearity. Numerical simulation seems to be the solution for predicting the mechanical behaviors of these types of structures rather than trying to find out closed-form analytical solutions. But even the numerical methods to the likes of FEM prove to be time-consuming in the cases of large deformation coupled multi-physical problems. This necessitates the development of an effective theoretical model for HMS structures. Various efforts have been made in the recent past to develop a theoretical model for HMS materials. A nonlinear field theory has been developed recently considering the coupling of magnetic field and finite deformation of HMS materials. The simulation was conducted using a FE software, the results of which agreed well with the experimental results [47]. Another study considered different volume fractions of the hard magnetic materials and studied the magnetization and shear moduli [54]. A magneto-visco-hyperelastic model was developed and calculations for simple deformations were performed using the FE method [55]. The dynamic features in HMS beams were also investigated [56]. Theoretical modeling of HMS beams considering extreme bending deformations was done and then solved analytically in a recent study [57].

Though recent studies have tried to understand the mechanics of the HMS structures, very little has been done to develop a theoretical model for the same without the use of any commercial software. Also as pointed out earlier these simulations are time-consuming due to the increased iterations owing to large deformation. The problem increases when dealing with dynamical parameters. In this section, we present a simple, effective and efficient theoretical model that accounts for the complex shape transition of the HMS structures by accommodating the exact expression for the curvature of the centerline. This will be used to model the unit cell of lattice materials (refer to the bottom-up framework presented in figures 1(A)–(E)), which will then be used for the evaluation of the five in-plane elastic constants of HMS hexagonal lattices. First, we would analyze the local-level deformation mechanics of the beam-like members accounting for both axial as well as bending deformation (refer to figure 1(E)). Then, we would consider a unit cell that is made up of such beam elements and analyze them to obtain the formulations of the five in-plane elastic constants in semi-analytical form. It is to be noted that at this point the impact of geometry of lattice microstructure is incorporated into the metamaterial design (refer to figures 1(C) and (D)). The effective elastic constants thus derived considering a unit cell are representative of the effective elastic properties of the entire lattice (refer to figure 1(D)), which could then be utilized in the design of various industrial structures as demonstrated in figures 1(A) and (B).

2.1. Deriving the governing equations for the HMS beam

Based on the requirement of analyzing the lattices under combined magneto-mechanical loading, we first develop the deformation physics of HMS beams under the combined application of magnetic field and mechanical loading. Note that analytical developments of HMS beams have not been undertaken under such combined loading in the literature. The HMS beam is analyzed using the Euler-Bernoulli beam theory, considering planar deformations. In the proposed theoretical model, the centerline of the beam may either be extensible or inextensible. The theoretical model is developed by deriving the governing equations in terms of the rotation angle, for the beam with both external load and magnetic field. The principle of minimum potential energy is used to derive the governing equations. Here the total strain energy U comprises magnetic potential energy U_M and elastic potential energy U_E.

Let us consider a HMS beam of length l, having a cross-sectional area A. The centerline strain is considered to be small, hence any change in A will be neglected. Let E be the intrinsic Young's modulus of the beam and I be the second moment of inertia. To account for the large deformation of the beam, its geometric exact nonlinearity needs to be considered. Thus, the stretch ratio λ and centerline rotation $\bar{\theta}$ are included in the formulation (refer to figure 1(E)). The axial and transverse displacements of the beam centerline are denoted by $\bar{u}$ and $\bar{v}$, respectively.

2.1.1. Magnetic potential energy of the HMS beam.

Let the residual magnetic flux density of the beam in the reference configuration be denoted as $B_0^{\bar{r}}$ and as $B^{\bar{r}}$ in the current configuration. The magnetic field applied externally be denoted by $B^{\bar{e}}$ and the angle that $B^{\bar{e}}$ makes with the horizontal line be $\bar{\alpha}$. The residual magnetic flux density is considered to be constant in magnitude and to be acting in the longitudinal direction or along the beam length. The magnetic potential energy per unit volume of the current configuration [47] is given as:

$$u_M = -\frac{1}{\mu_0} B^{\bar{r}}.B^{\bar{e}}, \tag{1}$$

where μ_0 represents the vacuum (or, air) permeability. The magnetic interaction due to the high residual magnetization and coercivity of the embedded hard-magnetic particles is captured by the above equation even for the very large deformations case. The residual magnetic flux density of the beam in the current configuration, i.e. $B^{\bar{r}}$ is given as:

$$B^{\bar{r}} = S|B_0^{\bar{r}}| \left[\cos\bar{\theta}\hat{\bar{i}} + \sin\bar{\theta}\hat{\bar{j}}\right], \tag{2}$$

Here S takes care of the non-uniform magnetization. Since we have assumed $B_0^{\bar{r}}$ to be constant and in longitudinal direction of the beam, so S can be either $+1$ (along $\bar{x}$—direction) or -1 (opposite to $\bar{x}$—direction) and may be considered as a coefficient. To capture complex deformation shapes of the beam, S can be designed as a function of the beam length, i.e. $S(\bar{x})$. The local beam axes are represented by $\bar{x}$ and $\bar{y}$ denoting axial and lateral directions, respectively. The externally applied magnetic field $B^{\bar{e}}$ is given as:

$$B^{\bar{e}} = |B^{\bar{e}}| \left[\cos\bar{\alpha}\hat{\bar{i}} + \sin\bar{\alpha}\hat{\bar{j}}\right]. \tag{3}$$

Now we substitute equations (2) and (3) into equation (1) to get:

$$u_M = -\frac{S}{\mu_0}|B_0^{\bar{r}}||B^{\bar{e}}|\cos\left(\bar{\theta} - \bar{\alpha}\right). \tag{4}$$

The magnetic potential energy of the beam can then be expressed as:

$$\begin{aligned} U_M &= \int_A \int_0^{\lambda l} u_m ds dA \\ &= -\frac{A}{\mu_0} \int_0^l S\lambda |B_0^{\bar{r}}||B^{\bar{e}}| \cos\left(\bar{\theta} - \bar{\alpha}\right) d\bar{x}. \end{aligned} \tag{5}$$

Using the relation between strain of the beam centreline ε and stretch ratio λ, $\varepsilon = \lambda - 1$, the above equation can be expressed as:

$$U_M = -\frac{A}{\mu_0} \int_0^l S(1+\varepsilon)|B_0^{\bar{r}}||B^{\bar{e}}| \cos\left(\bar{\theta} - \bar{\alpha}\right) d\bar{x}. \tag{6}$$

2.1.2. Elastic potential energy of the HMS beam. The total elastic potential energy of the beam, U_E consisting of membrane strain energy due to stretch of the beam's centerline, U_{mem} and the strain energy due to bending of the beam, U_{bend} is given as:

$$\begin{aligned} U_E &= U_{mem} + U_{bend} \\ &= A\int_0^l \Phi\, d\bar{x} + \frac{EI}{2}\int_0^l \left(\frac{d\bar{\theta}}{d\bar{x}}\right)^2 d\bar{x}, \end{aligned} \tag{7}$$

where Φ denotes the strain energy density function defined in per unit of the undeformed volume [58].

2.1.3. Priniciple of minimum potential energy. In this subsection we will derive the governing equations for the HMS beam considering both externally applied magnetic field and mechanical load using the principle of minimum potential energy. The variation of the magnetic potential energy, U_M (refer to equation (6)) is given as:

$$\begin{aligned} \partial U_M = &-\left(\frac{A}{\mu_0}\int_0^l S|B_0^{\bar{r}}||B^{\bar{e}}| \cos\left(\bar{\theta}-\bar{\alpha}\right) d\bar{x}\right) \partial\varepsilon \\ &+ \left(\frac{A}{\mu_0}\int_0^l S(1+\varepsilon)|B_0^{\bar{r}}||B^{\bar{e}}| \sin\left(\bar{\theta}-\bar{\alpha}\right) d\bar{x}\right) \partial\bar{\theta}. \end{aligned} \tag{8}$$

Similarly the variation of the elastic potential energy, U_E (refer to equation (7)) is given as:

$$\begin{aligned} \partial U_E &= A\int_0^l \partial\Phi\, d\bar{x} + EI\int_0^l \left(\frac{d\bar{\theta}}{d\bar{x}}\right)\left(\frac{d(\partial\bar{\theta})}{d\bar{x}}\right) d\bar{x} \\ &= \left(A\int_0^l \frac{d\Phi}{d\varepsilon} d\bar{x}\right)\partial\varepsilon + \left(EI\left(\frac{d\bar{\theta}}{d\bar{x}}\right)\Bigg|_0^l - EI\int_0^l \left(\frac{d^2\bar{\theta}}{d\bar{x}^2}\right) d\bar{x}\right)\partial\bar{\theta}. \end{aligned} \tag{9}$$

The HMS beam is considered to be acted upon by the following external loads namely, a distributed force with $\bar{p}(\bar{x})$ acting along $\bar{x}$-direction and $\bar{q}(\bar{x})$ acting along $\bar{y}$-direction, a distributed moment $\bar{m}(\bar{x})$ and a concentrated force $\vec{F} = F_{\bar{x}}\hat{\bar{i}} + F_{\bar{y}}\hat{\bar{j}}$ acting on the tip of the beam, i.e. at $\bar{x} = l$. Note that we have taken a generalized loading condition for the purpose of beam-level derivation here, among which some of the components would be considered as zero during the lattice-level derivation. The displacement vector at tip of the beam is $\vec{d} = \bar{u}\hat{\bar{i}} + \bar{v}\hat{\bar{j}}$. The variation of the work done by the external forces is given as:

$$\begin{aligned} \partial W &= \int_0^l \bar{p}\partial\bar{u} d\bar{x} + \int_0^l \bar{q}\partial\bar{v} d\bar{x} + \int_0^l \bar{m}\partial\bar{\theta} d\bar{x} + \vec{F}.\partial\vec{d} \\ &= \int_0^l \bar{p}\partial\bar{u} d\bar{x} + \int_0^l \bar{q}\partial\bar{v} d\bar{x} + \int_0^l \bar{m}\partial\bar{\theta} d\bar{x} + F_{\bar{x}}\partial\bar{u} + F_{\bar{y}}\partial\bar{v}. \end{aligned} \tag{10}$$

Note that equations (8)–(10) account for virtual displacements of four types, i.e. $\partial\bar{u}$, $\partial\bar{v}$, $\partial\bar{\theta}$ and $\partial\varepsilon$. In order to derive the governing equations and the boundary condition of the beam system, the redundant virtual displacements can be replaced and thus a unified problem with only two virtual displacements, namely, $\partial\bar{\theta}$ and $\partial\varepsilon$ can be setup. According to the Euler-Bernoulli framework, we can relate the four virtual displacements using two equations (or two constraints) and this reduces the problem to two virtual displacements (two variables) which simplifies the problem under consideration. The geometric relationships between $\bar{u}$, $\bar{v}$, $\bar{\theta}$ and ε, are given as:

$$\frac{d\bar{u}}{d\bar{x}} = \lambda\cos\bar{\theta} - 1 = (1+\varepsilon)\cos\bar{\theta} - 1 \tag{11a}$$

$$\frac{d\bar{v}}{d\bar{x}} = \lambda\sin\bar{\theta} = (1+\varepsilon)\sin\bar{\theta}. \tag{11b}$$

The value of displacements at $\bar{x} = 0$ are fixed as zero, to eliminate the effect of rigid body displacement of the system. The centerline displacements are then given as:

$$\bar{u} = \int_0^{\bar{x}} (1+\varepsilon)\cos\bar{\theta} d\bar{x} - \bar{x} \tag{12a}$$

$$\bar{v} = \int_0^{\bar{x}} (1+\varepsilon)\sin\bar{\theta} d\bar{x}. \tag{12b}$$

The variation of equations (12*a*) and (12*b*) gives:

$$\partial\bar{u} = \left(\int_0^{\bar{x}} \cos\bar{\theta} d\bar{x}\right)\partial\varepsilon - \left(\int_0^{\bar{x}} (1+\varepsilon)\sin\bar{\theta} d\bar{x}\right)\partial\bar{\theta} \tag{13a}$$

$$\partial\bar{v} = \left(\int_0^{\bar{x}} \sin\bar{\theta} d\bar{x}\right)\partial\varepsilon + \left(\int_0^{\bar{x}} (1+\varepsilon)\cos\bar{\theta} d\bar{x}\right)\partial\bar{\theta}. \tag{13b}$$

Substituting the equations (13*a*) and (13*b*) into equation (10) gives:

$$\begin{aligned} &\partial W \\ &= \begin{pmatrix} \int_0^l \bar{p}\left(\int_0^{\bar{x}} \cos\bar{\theta} d\bar{x}\right) d\bar{x} + \int_0^l \bar{q}\left(\int_0^{\bar{x}} \sin\bar{\theta} d\bar{x}\right) d\bar{x} \\ +F_{\bar{x}}\int_0^l \cos\bar{\theta} d\bar{x} + F_{\bar{y}}\int_0^l \sin\bar{\theta} d\bar{x} \end{pmatrix}\partial\varepsilon \\ &\quad - \begin{pmatrix} \int_0^l \bar{p}\left(\int_0^{\bar{x}} (1+\varepsilon)\sin\bar{\theta} d\bar{x}\right) d\bar{x} - \int_0^l \bar{q}\left(\int_0^{\bar{x}} (1+\varepsilon)\cos\bar{\theta} d\bar{x}\right) d\bar{x} \\ -\int_0^l \bar{m} d\bar{x} + F_{\bar{x}}\int_0^l (1+\varepsilon)\sin\bar{\theta} d\bar{x} - F_{\bar{y}}\int_0^l (1+\varepsilon)\cos\bar{\theta} d\bar{x} \end{pmatrix}\partial\bar{\theta}. \end{aligned} \tag{14}$$

Note that the above equation is expressed in terms of only two virtual displacements, $\partial\varepsilon$ and $\partial\bar{\theta}$. Now using the following integral property [59]:

$$\int_0^l g(\bar{x})\left(\int_0^{\bar{x}} f(\bar{x})\,\partial\bar{\theta}d\bar{x}\right)d\bar{x} = \int_0^l \left(\int_{\bar{x}}^l g(\bar{x})\,d\bar{x}\right) f(\bar{x})\,\partial\bar{\theta}d\bar{x}, \tag{15}$$

the equation (14) can be rewritten as:

$$\begin{aligned}\partial W &\\ = &\begin{pmatrix}\int_0^l\left(\int_{\bar{x}}^l\bar{p}d\bar{x}\right)\cos\bar{\theta}d\bar{x}+\int_0^l\left(\int_{\bar{x}}^l\bar{q}d\bar{x}\right)\sin\bar{\theta}d\bar{x}\\ +F_{\bar{x}}\int_0^l\cos\bar{\theta}d\bar{x}+F_{\bar{y}}\int_0^l\sin\bar{\theta}d\bar{x}\end{pmatrix}\partial\varepsilon\\ &-\begin{pmatrix}\int_0^l\left(\int_{\bar{x}}^l\bar{p}d\bar{x}\right)(1+\varepsilon)\sin\bar{\theta}d\bar{x}-\int_0^l\left(\int_{\bar{x}}^l\bar{q}d\bar{x}\right)(1+\varepsilon)\cos\bar{\theta}d\bar{x}\\ -\int_0^l\bar{m}d\bar{x}+F_{\bar{x}}\int_0^l(1+\varepsilon)\sin\bar{\theta}d\bar{x}-F_{\bar{y}}\int_0^l(1+\varepsilon)\cos\bar{\theta}d\bar{x}\end{pmatrix}\partial\bar{\theta}.\end{aligned} \tag{16}$$

The principle of minimum potential energy gives:

$$\partial(U-W)=0 \tag{17}$$

here $U=U_M+U_E$. Therefore the above equation becomes:

$$\begin{gathered}\partial(U_M+U_E-W)=0\\ \partial U_M+\partial U_E-\partial W=0\end{gathered} \tag{18}$$

Inserting equations (8), (9) and (16) into equation (18) gives two governing equations, one involving $\partial\varepsilon$ and the other involving $\partial\bar{\theta}$. $\partial\varepsilon$:

$$\begin{aligned}&A\left(\sigma_N-\frac{S}{\mu_0}|B_0^{\bar{r}}||B^{\bar{e}}|\cos\left(\bar{\theta}-\bar{\alpha}\right)\right)-\left(\int_{\bar{x}}^l\bar{p}d\bar{x}\right)\cos\bar{\theta}\\ &-\left(\int_{\bar{x}}^l\bar{q}d\bar{x}\right)\sin\bar{\theta}-F_{\bar{x}}\cos\bar{\theta}-F_{\bar{y}}\sin\bar{\theta}=0.\end{aligned} \tag{19}$$

$\partial\bar{\theta}$:

$$\begin{aligned}&EI\left(\frac{d^2\bar{\theta}}{d\bar{x}^2}\right)-\frac{AS}{\mu_0}(1+\varepsilon)|B_0^{\bar{r}}||B^{\bar{e}}|\sin\left(\bar{\theta}-\bar{\alpha}\right)\\ &-\left(\int_{\bar{x}}^l\bar{p}d\bar{x}\right)(1+\varepsilon)\sin\bar{\theta}+\left(\int_{\bar{x}}^l\bar{q}d\bar{x}\right)(1+\varepsilon)\cos\bar{\theta}\\ &+\bar{m}-F_{\bar{x}}(1+\varepsilon)\sin\bar{\theta}+F_{\bar{y}}(1+\varepsilon)\cos\bar{\theta}=0,\end{aligned} \tag{20}$$

with the following boundary conditions (adopted based on lattice-level periodicity):

$$\bar{\theta}=0 \quad \text{at} \quad \bar{x}=0 \quad \text{and} \quad \bar{x}=l, \tag{21}$$

here $\sigma_N=\left(\frac{d\Phi}{d\varepsilon}\right)$ denotes the nominal stress. To simplify the governing equations and solve the beam model, we will introduce the following non-dimensional quantities that will make the results more general:

$$\begin{gathered}\bar{\xi}=\frac{\bar{x}}{l};\quad \bar{\zeta}=\frac{\bar{u}}{l};\quad \bar{\eta}=\frac{\bar{v}}{l};\quad \Pi=\frac{Al^2}{I};\quad B=\frac{|B_0^{\bar{r}}||B^{\bar{e}}|\Pi}{E\mu_0};\\ P=\frac{\bar{p}l^3}{EI};\quad Q=\frac{\bar{q}l^3}{EI};\quad \bar{M}=\frac{\bar{m}l^2}{EI};\quad \bar{F}_{\bar{x}}=\frac{F_{\bar{x}}l^2}{EI};\\ \bar{F}_{\bar{y}}=\frac{F_{\bar{y}}l^2}{EI};\quad \bar{\sigma}_N=\frac{\sigma_N}{E}=\frac{\frac{d\Phi}{d\varepsilon}}{E}\end{gathered} \tag{22}$$

Equations (19) and (20), after non-dimensionalization using parameters of equation (22), are thus expressed as:

$$\begin{aligned}&A\bar{\sigma}_N-BS\cos\left(\bar{\theta}-\bar{\alpha}\right)-\left(\int_{\bar{\xi}}^1 Pd\bar{\xi}\right)\cos\bar{\theta}\\ &-\left(\int_{\bar{\xi}}^1\bar{Q}d\bar{\xi}\right)\sin\bar{\theta}-\bar{F}_{\bar{x}}\cos\bar{\theta}-\bar{F}_{\bar{y}}\sin\bar{\theta}=0,\end{aligned} \tag{23}$$

and

$$\begin{aligned}&\left(\frac{d^2\bar{\theta}}{d\bar{\xi}^2}\right)-BS(1+\varepsilon)\sin\left(\bar{\theta}-\bar{\alpha}\right)-\left(\int_{\bar{\xi}}^1\bar{P}d\bar{\xi}\right)(1+\varepsilon)\sin\bar{\theta}\\ &+\left(\int_{\bar{\xi}}^1\bar{Q}d\bar{\xi}\right)(1+\varepsilon)\cos\bar{\theta}+\bar{M}-\bar{F}_{\bar{x}}(1+\varepsilon)\sin\bar{\theta}\\ &+\bar{F}_{\bar{y}}(1+\varepsilon)\cos\bar{\theta}=0.\end{aligned} \tag{24}$$

2.1.4. *Inextensible HMS beam model.*

For an inextensible beam, the centerline strain is zero. Thus the governing equation for an inextensible HMS beam model can be obtained by putting $\varepsilon=0$ in equation (24) (while the equation (23) can be ignored since the variation of centerline strain is not meaningful for inextensible beams):

$$\begin{aligned}&\left(\frac{d^2\bar{\theta}}{d\bar{\xi}^2}\right)-BS\sin\left(\bar{\theta}-\bar{\alpha}\right)-\left(\int_{\bar{\xi}}^1\bar{P}d\bar{\xi}\right)\sin\bar{\theta}\\ &+\left(\int_{\bar{\xi}}^1\bar{Q}d\bar{\xi}\right)\cos\bar{\theta}+\bar{M}-\bar{F}_{\bar{x}}\sin\bar{\theta}+\bar{F}_{\bar{y}}\cos\bar{\theta}=0\end{aligned} \tag{25}$$

2.1.5. *Solving the coupled set of equations.*

The equations (23) and (24) are coupled equations where the first equation is a non-linear equation whereas the second equation is a second-order differential equation. This non-linearity in the equations arises from the inherent geometric and material non-linearities due to the beam curvature and the material properties respectively. Previously, the Galerkin method has been used by effectively discretizing the infinite dimensional beam [60, 61]. This simplifies the complex set of coupled non-linear equations into two sets of a linear system of equations by choosing a base function set that is complete. This method proves to be more complicated to solve when the current generic beam is considered involving both mechanical and magnetic loading. Hence, we deploy an intuitive method that can give us both $\varepsilon(\bar{x})$ and $\bar{\theta}(\bar{x})$ from the non-linear set of governing equations, as discussed in the following subsection.

2.1.6. Numerical model for solving the coupled differential equations. The two governing equations can be solved using the boundary conditions from equation (21) to get $\bar{\theta}(\bar{x})$. To obtain $\varepsilon(\bar{x})$ from the coupled equations we generally need two more boundary conditions resulting from the application of the external loads; but in our approach, we use an intuitive numerical method by which we can obtain the function $\varepsilon(\bar{x})$ without the necessity of the two boundary conditions resulting from the external loads.

In the analyses of HMS beams, we generally have an idea of the range of the values that ε can lie within. This is what we mainly exploit in our approach. The 'inextensibility assumption' as discussed by [60] evaluates the maximum force that can be applied is 500 N, which stems from the fact that they consider a maximum ε value 0.05. Beyond this the assumption becomes invalid. Since all our analyses are based on the magnitude of forces well within the range of 100 N, we consider a broad range of $\varepsilon = [0.00004, 0.01]$.

We follow the following steps in solving the governing equations. Firstly, we split the governing equations in (23) and (24) into a primary and a secondary equations. The differential equation in equation (24) serves as our 'Primary equation'. We solve this equation for orderly increasing values of ε to get a corresponding $\bar{\theta}$ vs $\bar{\xi}$. The non-linear equation in (23) serves as our 'Secondary equation'. Since we have a coupled set of equations the result from our Primary equation must satisfy the non-linear Secondary equation. Subsequently, we iterate over 100 values in the range $[0, 1]$ of $\bar{\xi}$. This is mainly done to get a corresponding mapping from $\bar{\xi}$ to $[\bar{\theta} \quad \text{and} \quad \varepsilon]$ for all the iterations and thus obtain a very good estimate of the functions $[\bar{\theta}(\bar{\xi}) \quad \text{and} \quad \varepsilon(\bar{\xi})]$.

For each such value of $\bar{\xi}$, we then iterate over a range of values of ε (preferably 100 values) and obtain the corresponding data of $\bar{\theta}$ vs $\bar{\xi}$ for all these iterations by solving the Primary equation using 'bvp4c' function in MATLAB for solving boundary value problems (with a rotationally restrained boundary condition at both ends; refer to equation (21). From the $\bar{\theta}$ vs $\bar{\xi}$ data we obtain the value of $\bar{\theta}$ for the current iteration's $\bar{\xi}$ and then retain the value. Then, during each of these iterations, we calculate the value of the left-hand side of the Primary equation and then find the ε value which minimizes the left-hand side of the Secondary equation. This gives us a value for both $\bar{\theta}$ and ε for each iteration over $\bar{\xi}$s in $[0, 1]$. Thus we now obtain the functional mapping using numerical data from $\bar{\xi}$ to both $\bar{\theta}$ and ε.

For analyzing hexagonal lattices maintaining unit cell level periodic boundary conditions, we need to analyze beams with one end fixed and the other end rotationally restrained condition, while applying a transverse point load at the rotationally restrained end and a magnetic field in any arbitrary orientation. A computational framework of the beam with this boundary and loading condition is sufficient for the subsequent lattice-level analysis (in-plane) for evaluating the two Young's moduli, two Poisson's ratios and shear modulus. In the further analysis, since our focus is solely on the magnetic field and concentrated load, we set $\bar{P} = \bar{Q} = \bar{M} = 0$ and $\bar{\sigma}_N = \varepsilon$.

2.2. Effective in-plane elastic properties of active hexagonal lattices

The effective mechanical properties of the proposed active lattice-based material are defined as a function of the unit cell geometry, intrinsic material properties of the beam-like members (including the multi-physical properties of the hard magnetic particles) and applied magnetic field. The lattice here is conceived as a periodic beam network. Since the deformation physics of the constituting beams is active in nature and depends on the applied magnetic field, the global deformation behavior of the lattice becomes a function of the applied magnetic field. Subsequently, the effective elastic properties of the lattice can be actively modulated as a function of the magnetic field and applied external mechanical stress. Note that since we consider large nonlinear deformation of the lattices, the effective elastic properties become dependent on the lattice-level externally applied remote stress. The active component in the proposed lattice metamaterial can be controlled through the intensity and direction of magnetic fields, while the influence of magnetic fields can be accentuated based on the distribution and orientation of the hard magnetic particles within the beam-like members. In this article, we consider an external magnetic field actuation acting in direction-2 of the lattice (refer to figure 2), where beams have uniformly distributed hard magnetic particles.

In this section, the deflection values at the beam-level obtained using the numerical model (as described in the preceding subsection) are used to further evaluate the homogenized effective elastic properties ($E_1, E_2, \nu_{12}, \nu_{21}$ and G_{12}) at the lattice level, considering a unit cell-based approach. To take care of the effect of large deformation analysis, we consider incremental geometry updation at the unit cell level [62]. The initial configuration S^0 of hexagonal honeycomb is considered to be no-load configuration having load step dependent cell walls of length l_s^0 and inclination angle θ^0 (refer to figures 2(A) and 3(A)). At ith load step, in the deformed configuration S^i, the load step dependent length and inclination angle of the cell walls become l_s^i and θ^i, respectively. Note that we consider the width b and thickness t of all cell walls to be independent of the load step (refer to figures 2(B) and (C)).

2.2.1. Longitudinal young's modulus E_1. To derive the non-linear longitudinal Young's modulus, we consider a uniform incremental compressive stress field $\sigma_1^i (= \sigma_1^{i-1} + \Delta\sigma_1^i)$ being applied to the unit cell along direction-1 (i.e. in the longitudinal direction). This stress produces a force P_i that acts at the beam end points (refer to figure 2(D)). The equivalent force P_i acting on the beam end can be expressed as:

$$P_i = \sigma_1^i b (h + l_s^{i-1} \sin\theta^{i-1}). \tag{26}$$

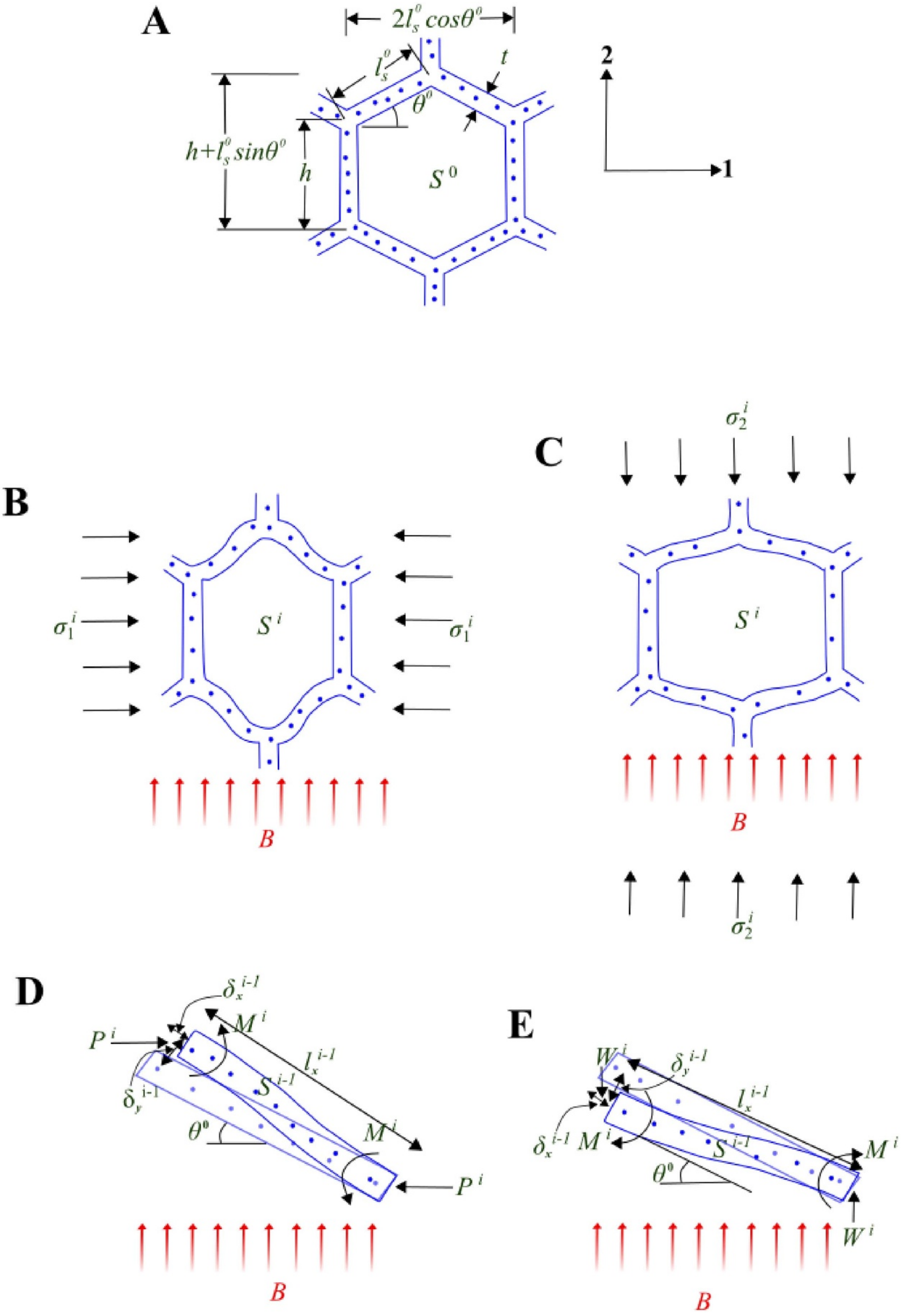

Figure 2. Mechanics of unit cells under the coupled effect of normal mechanical stress and magnetic field. (A) Undeformed honeycomb at initial configuration S^0, with ferromagnetic materials embedded inside. (B) Deformed configuration of the honeycomb under the stress field σ_1. (C) Deformed configuration of the honeycomb under the stress field σ_2. (D) Free-body diagram of a HMS beam element under the stress field σ_1 acting along the longitudinal direction. The longitudinal Young's modulus E_1 and the Poisson's ratio ν_{12} are derived using this configuration. (E) Free-body diagram of a HMS beam element under the stress field σ_2 acting along the lateral direction. The longitudinal Young's modulus E_2 and the Poisson's ratio ν_{21} are derived using this configuration. Note that the vertical cell walls remain unaffected by the magnetic field actuation in all configurations and it is independent of the load step.

We substitute this force and the externally applied magnetic flux density B (non-dimensional quantity representing the magnetic actuation) in the governing equations (refer to equations (23) and (24)), which are then solved using the above described numerical model to get axial deformation δ_x^i and transverse deformation δ_y^i at the tip of the beam under the influence of both B and P_i. The boundary condition of the beams is considered as one end fixed and the other end rotationally restrained. The moment M^i that bends the cell wall (refer figure 2(D)) is given as:

$$M^i = \frac{P^i \sin\theta^0 l_x^{i-1} + P^i \cos\theta^0 \delta_y^{i-1}}{2}, \tag{27}$$

where l_x^i and l_s^i are related by:

$$l_s^i = \sqrt{\left(l_x^i\right)^2 + \left(\delta_y^i\right)^2} \tag{28}$$

Total deflection in direction -1 is given as:

$$\delta_1^i = \delta_y^i \sin\theta^0 + \delta_x^i \cos\theta^0. \tag{29}$$

Strain along the direction of σ_1^i is given as:

$$\varepsilon_1^i = \delta_1^i / l_s^0 \cos\theta^0. \tag{30}$$

Note that we calculate the strain with respect to the reference configuration S^0. Now the longitudinal Young's modulus can be expressed as (corresponding to ith increment):

$$E_1 = \frac{\sigma_1^i}{\varepsilon_1^i} = \frac{l_s^0 \cos\theta^0 \sigma_1^i}{\delta_y^i \sin\theta^0 + \delta_x^i \cos\theta^0}. \tag{31}$$

2.2.2. Poisson's ratio ν_{12}. To obtain Poisson's ratio ν_{12}, we calculate the strain in direction 2 resulting from the stress σ_1^i acting along the direction-1 as shown in figure 2(D). The total deflection in direction-2 (δ_2) is obtained as:

$$\delta_2^i = \delta_y^i \cos\theta^0 - \delta_x^i \sin\theta^0. \tag{32}$$

Now, the total strain along direction-2 is given as:

$$-\varepsilon_2^i = \frac{\delta_2^i}{h + l_s^0 \sin\theta^0}. \tag{33}$$

From the equations (30) and (33), the Poisson's ratio ν_{12} is given as:

$$\nu_{12} = -\frac{\varepsilon_2^i}{\varepsilon_1^i} = \frac{l_s^0 \cos\theta^0 \left(\delta_y^i \cos\theta^0 - \delta_x^i \sin\theta^0\right)}{\left(h + l_s^0 \sin\theta^0\right)\left(\delta_y^i \sin\theta^0 + \delta_x^i \cos\theta^0\right)}. \tag{34}$$

2.2.3. Transverse Young's modulus E_2. To obtain the nonlinear transverse Young's modulus E_2, we consider a uniform incremental compressive stress field $\sigma_2^i (= \sigma_2^{i-1} + \Delta\sigma_2^i)$ in direction-2 being applied on the unit cell. This results in a vertical force W_i at the end points (refer to figure 2(E)). W_i is expressed as:

$$W_i = \sigma_2^i b l_s^{i-1} \cos\theta^{i-1}. \tag{35}$$

We substitute this force and the externally applied magnetic flux density B in the governing equations (refer to equations (23) and (24)), which are then solved using the above described numerical model to get axial deformation δ_i^x and transverse deformation δ_i^y at the tip of the beam under the influence of both $B^{\bar{e}}$ and W_i. The boundary condition of the beams is considered as one end fixed and the other end rotationally restrained. The total lateral force (acting in direction-2) at point O is $2W_i$, accounting for the axial deformation of the vertical member OC. The moment M^i obtained from the free body diagram in figure 2(E) is given as:

$$M^i = \frac{W^i \cos\theta^0 l_x^{i-1} + W^i \sin\theta^0 \delta_y^{i-1}}{2}. \tag{36}$$

Total deflection, therefore, in direction-2 is given as:

$$\delta_2^i = \delta_y^i \cos\theta^0 + \delta_x^i \sin\theta^0 + \frac{2hl_s^0 \cos\theta^0 \sigma_2^i}{tE}. \tag{37}$$

The strain in direction-2 can be expressed as:

$$\varepsilon_2^i = \frac{\delta_2^i}{h + l_s^0 \sin\theta^0}. \tag{38}$$

Thus, transverse Young's modulus acting along direction-2 (i.e. the transverse direction) corresponding to the ith increment is given as:

$$E_2 = \frac{\sigma_2^i}{\varepsilon_2^i} = \frac{\left(h + l_s^0 \sin\theta^0\right)\sigma_2^i}{\delta_y^i \cos\theta^0 + \delta_x^i \sin\theta^0 + \dfrac{2hl_s^0 \cos\theta^0 \sigma_2^i}{tE}}. \tag{39}$$

2.2.4. Poisson's ratio ν_{21}. For quantifying the Poisson's ratio ν_{21}, we need to obtain the strain in direction 1, resulting from the stress applied along the direction-2. The deformation along direction-1 (i.e. in the longitudinal direction) due to σ_2^i is given as (refer to figure 2(E)):

$$\delta_1^i = \delta_y^i \sin\theta^0 - \delta_x^i \cos\theta^0. \tag{40}$$

Thus, strain due to the above calculated deflection in direction-1 can then be given as:

$$-\varepsilon_1^i = \frac{\delta_1^i}{l_s^0 \cos\theta^0}. \tag{41}$$

From the equations (38) and (41), the Poisson's ratio ν_{21} can be expressed as:

$$\nu_{21} = -\frac{\varepsilon_1^i}{\varepsilon_2^i} = \frac{\left(h + l_s^0 \sin\theta^0\right)\left(\delta_y^i \sin\theta^0 - \delta_x^i \cos\theta^0\right)}{l_s^0 \cos\theta^0 \left(\delta_y^i \cos\theta^0 + \delta_x^i \sin\theta^0 + \dfrac{2hl_s^0 \cos\theta^0 \sigma_2^i}{tE}\right)}. \tag{42}$$

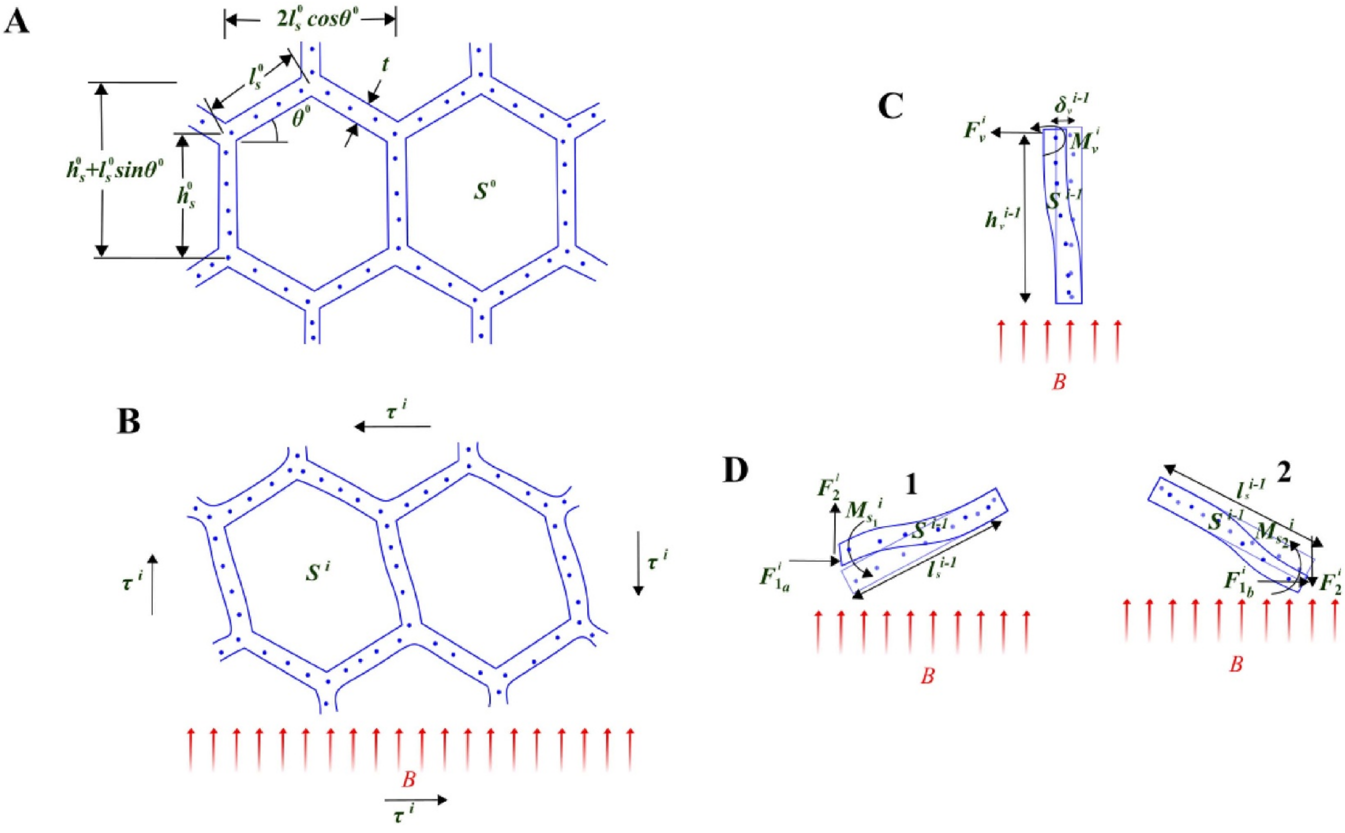

Figure 3. Mechanics of unit cells under the coupled effect of shear stress and magnetic field. (A) Undeformed honeycomb at initial configuration S^0, with ferromagnetic materials embedded inside. (B) Deformed configuration of the honeycomb under the shear stress field τ. (C) Free-body diagram of a vertical cell wall of the honeycomb under the stress (shear) field τ. (D) Free-body diagram of the slant cell walls (1 and 2) of the honeycomb under the stress field τ. Both these configurations (C and D) are used for the derivation of shear modulus G_{12}.

2.2.5. Shear modulus G_{12}. To derive of the shear modulus G_{12}, we consider the shear strain arising from the bending deformations as well as that due to axial deformations. For the case of shear modulus, the vertical cell walls are also considered to be load step dependent. In the initial configuration S^0 of hexagonal honeycomb, the vertical cell wall is considered to have length h_s^0 while the slant cell walls have length l_s^0 and inclination angle is θ^0 (refer to figure 3(A)). At ith load step, in the deformed configuration S^i (refer to figure 3(B)), the load step dependent length of the vertical cell wall becomes h_s^i and that of slant cell walls and their inclination angle become l_s^i and θ^i, respectively. The deformation occurs under the effect of anti-clockwise mode of incremental shear stress $\tau^i(=\tau^{i-1}+\Delta\tau^i)$, as considered in the current analysis (note that the shear moduli under a given magnetic field would be same for clock-wise and anti-clockwise modes for the current scenario). This shear stress field produces forces F_1^i and F_2^i in the slant members, which are given as (refer to figure 3(D)):

$$F_1^i = 2\tau^i b l_s^{i-1}\cos\theta^{i-1} \tag{43a}$$

$$F_2^i = \tau^i b\left(h_s^{i-1}+l_s^{i-1}\sin\theta^{i-1}\right). \tag{43b}$$

The force produced in the vertical cell member is given as (refer to figure 3(C)):

$$F_v^i = F_1^i = 2\tau^i b l_s^{i-1}\cos\theta^{i-1}. \tag{44}$$

The moment M_v^i generated in the vertical member at both the ends (refer to figure 3(C)) is given as:

$$M_v^i = \frac{F_1^i h_v^{i-1}}{2}. \tag{45}$$

No axial force is produced in the vertical cell wall under the applied shear stress. This moment M_v gets distributed in the two slant members. Note that the two slant members deform differently depending on the external magnetic force B. At certain portion of a particular slant member, B acts along the deformation caused due to mechanical stress and in other portion it acts in opposite direction to the applied stress resulting in different deformation of the two slant members. Thus the moment M_v does not get distributed equally on the two slant cell walls. The moment generated on slant member 1 is denoted by $M_{s_1}^i$ while that on the slant member 2 is $M_{s_2}^i$ (refer to figure 3(D)). The sum of the two moments is equal to M_v, i.e. $M_v = M_{s_1}^i + M_{s_2}^i$. Thus we see that the externally applied magnetic flux density B causes different deformation of the slant members making it an asymmetric problem. The force F_1^i gets distributed on both the slant members as $F_{1_a}^i$ and $F_{1_b}^i$ such that $F_1^i = F_{1_a}^i + F_{1_b}^i$. Note that these forces act in conjunction with the externally applied magnetic flux density B. We use the components of these forces ($F_{1_a}^i$, $F_{1_b}^i$ and F_2^i) acting on the slant members along the axial and transverse directions. Using these external loads the governing equations (refer to equations (23) and (24)) are solved based on the numerical model discussed previously. The numerical model gives the tip deflections, namely, transverse deflection δ_v^i of the vertical member, axial deflections $\delta_{x_1}^i$, $\delta_{x_2}^i$ and transverse deflections $\delta_{y_1}^i$, $\delta_{y_2}^i$ of the slant members 1 and 2, respectively. The total shear strain γ_t^i arising under the incremental shear stress τ^i and B comprises of the shear strain of vertical cell wall γ_v^i and that of the slant cell walls γ_s^i. The shear deflection of the vertical cell wall arises due to the transverse deflection δ_v^i of the vertical cell wall and its rotation ϕ^i, which arises from the bending deformations $\delta_{y_1}^i$ and $\delta_{y_2}^i$ of the slant cell walls. For our analysis, we find the individual values of $F_{1_a}^i$ and $F_{1_b}^i$ numerically so that $F_1^i = F_{1_a}^i + F_{1_b}^i$ along with satisfying the other compatibility condition pertaining to the rotation of the slant members 1 and 2 and vertical member. The rotation of the vertical cell wall and that of the slant members will be same to maintain the integrity of the structure, i.e. $\phi^i = \phi_1^i = \phi_2^i$. Here ϕ_1^i and ϕ_2^i are the rotations of the slant members, which are given as:

$$\phi_1^i = \tan^{-1}\left(\delta_{y_1}^i / l_x^i\right) \text{ and } \phi_2^i = \tan^{-1}\left(\delta_{y_2}^i / l_x^i\right), \tag{46}$$

where l_x^i and l_s^i are related by:

$$l_s^i = \sqrt{(l_x^i)^2 + \left(\delta_{y_{1(/2)}}^i\right)^2}. \tag{47}$$

Thus the shear strain γ_v^i of the vertical cell wall in the diretion of applied incremental shear stress τ^i is given as:

$$\gamma_v^i = \frac{\phi_i h_s^0 + \delta_v^i}{h_s^0 + l_s^0 \sin\theta^0}. \tag{48}$$

The shear strain γ_s^i of the slant cell wall in the direction of applied incremental shear stress τ^i is given as:

$$\gamma_s^i = \frac{\delta_{x_1}^i \sin\theta^0 + \delta_{x_2}^i \sin\theta^0}{l_s^0 \cos\theta^0} + \frac{\delta_{x_1}^i \cos\theta^0 + \delta_{x_2}^i \cos\theta^0}{h_s^0 + l_s^0 \sin\theta^0}. \tag{49}$$

The total shear strain γ_t^i is therefore given by:

$$\gamma_t^i = \gamma_v^i + \gamma_s^i = \frac{\phi_i h_s^0 + \delta_v^i + \delta_{x_1}^i \cos\theta^0 + \delta_{x_2}^i \cos\theta^0}{h_s^0 + l_s^0 \sin\theta^0} + \frac{\delta_{x_1}^i \sin\theta^0 + \delta_{x_2}^i \sin\theta^0}{l_s^0 \cos\theta^0}. \tag{50}$$

The shear modulus G_{12} can, therefore, be expressed as:

$$G_{12} = \frac{\tau^i}{\gamma_t^i} = \frac{\tau^i}{\dfrac{\phi_i h_s^0 + \delta_v^i + \delta_{x_1}^i \cos\theta^0 + \delta_{x_2}^i \cos\theta^0}{h_s^0 + l_s^0 \sin\theta^0} + \dfrac{\delta_{x_1}^i \sin\theta^0 + \delta_{x_2}^i \sin\theta^0}{l_s^0 \cos\theta^0}}. \tag{51}$$

Note that in this analysis, we have considered anticlockwise shear stress. When the shear stress acts in the clockwise sense, the slant members 1 and 2 behave opposite to the present anticlockwise shear case, but the total shear strain under a specific value of shear stress remains the same. Thus the shear modulus is same in both cases. This is unlike the case for E_1, E_2, ν_{12} and ν_{21} which change under tensile and compressive stress fields.

The expressions of five in-plane effective elastic moduli are presented in equations (31), (34), (39), (42) and (51). A careful consideration of these equations would reveal that the elastic moduli depend on different deflection components and the applied far-field stress. The deflection components further depend on the applied far-field stress (mechanical loading) and magnetic field. Thus the effective elastic properties under a certain value of applied stress are functions of the magnetic field, leading to an on-demand active modulation capability.

2.3. *Elastic moduli considering only the bending deformation*

In the preceding subsection, we have presented the generic framework for evaluating the nonlinear elastic properties considering both axial and transverse deflections of the beam-like elements. The five in-plane elastic moduli, considering only the bending deformation (ignoring the axial deformation part), i.e., $\delta_x^i = 0$, based on the previously derived equations (refer equations (31), (34), (39), (42), (51)) lead to:

$$E_1 = \frac{l_s^0 \cos\theta^0 \sigma_1^i}{\delta_y^i \sin\theta^0} \tag{52a}$$

$$\nu_{12} = \frac{l_s^0 \cos^2\theta^0}{(h + l_s^0 \sin\theta^0)\sin\theta^0} \tag{52b}$$

$$E_2 = \frac{\left(h + l_s^0 \sin\theta^0\right)\sigma_2^i}{\delta_y^i \cos\theta^0} \tag{52c}$$

$$\nu_{21} = \frac{\left(h + l_s^0 \sin\theta^0\right)\sin\theta^0}{l_s^0 \cos^2\theta^0} \tag{52d}$$

$$G_{12} = \frac{\tau^i}{\dfrac{\phi_i h_s^0 + \delta_v^i}{h_s^0 + l_s^0 \sin\theta^0}}. \tag{52e}$$

The above expressions are useful in the case of axially rigid beams, where the axial deformation can be neglected because of dominant bending deformation [15]. So the axial deformation in these structures can be neglected, which in our case will lead to low-density thin-walled honeycombs. It is interesting to note that the Poisson's ratios (ν_{12} and ν_{21}) for such lightweight honeycomb lattices are independent of the external loads. When the beam-like cell walls are assumed to be axially rigid (i.e. the axial deformations are neglected), we find that the Poisson's ratios are dependent only on the geometry of the microstructure. These observations agree with those available in literature [36, 63, 64], in which the impact of other multi-physical behaviors is considered.

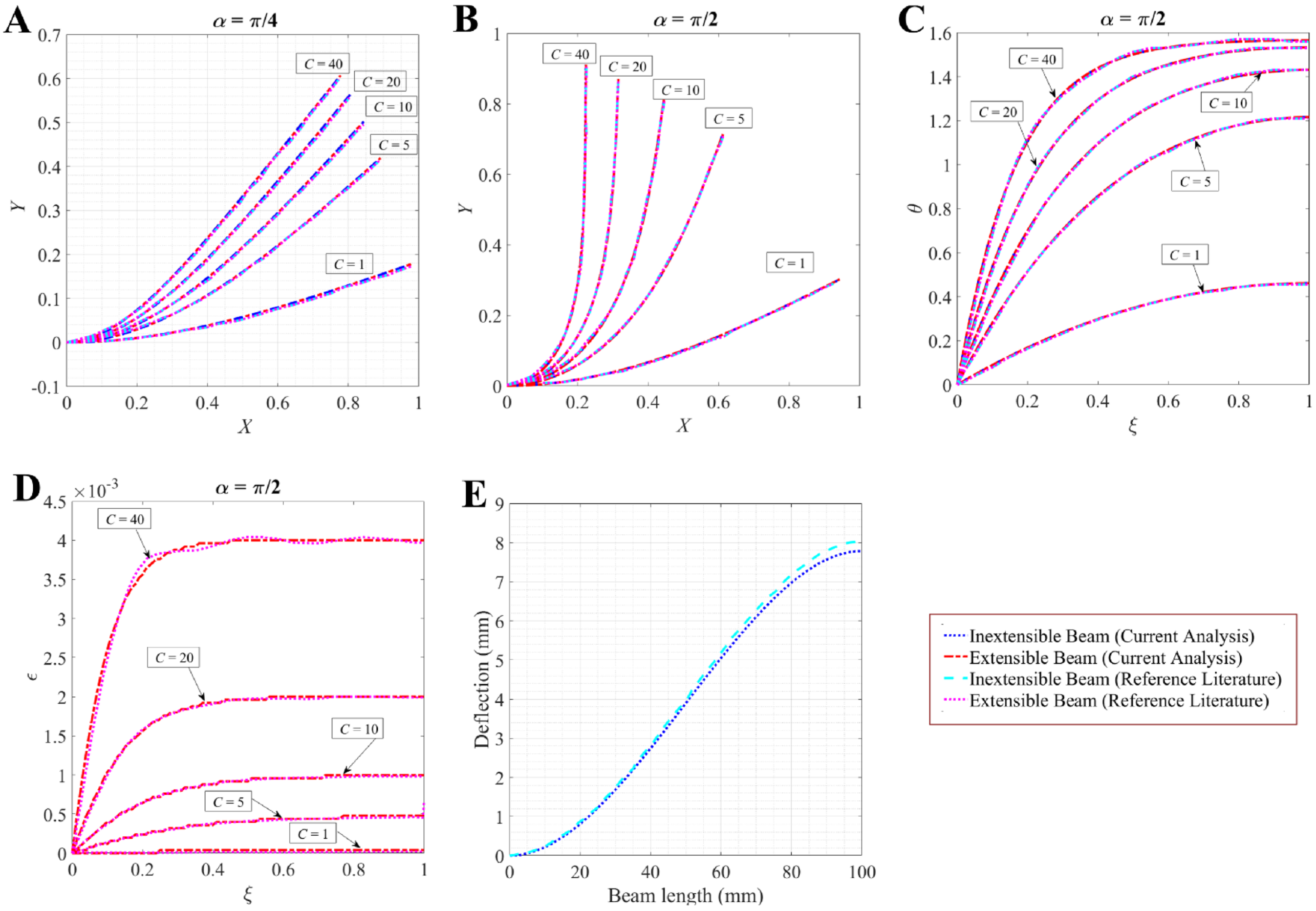

Figure 4. Numerical validation for a nonlinear beam element with only mechanical load and no magnetic flux density. (A) Comparison of the deformed configurations according to the inextensible and extensible beam models when $\alpha = \pi/4$, with the reference literature [60]. (B) Comparison of the deformed configurations according to the inextensible and extensible beam models when $\alpha = \pi/2$, with the reference literature [60]. (C) Comparison of the rotation angle according to the inextensible and extensible beam models when $\alpha = \pi/2$, with the reference literature [60]. (D) Comparison of the strain for the extensible beam model when $\alpha = \pi/2$, with the reference literature [60]. Here C and α, as used in the reference literature, are normalized force at the tip of the cantilevered beam and the angle between the force direction and the local beam axis, respectively. (E) Comparison of displacement field using the numerical model with the reference literature considering both end rotationally restrained boundary condition (as necessary for the current unit cell level analysis) [62].

3. Results and discussion

In this section we will present numerical results to characterize the effect of magnetic field intensity comprehensively following the numerical model proposed in the section above. Before moving forward with the numerical investigation, the validity of the numerical model for a HMS beam under the effect of both mechanical load and magnetic flux density (refer to section 2.1.6), needs to be established. The validated numerical model is then used for the quantification of the elastic moduli of lattice-based structure. At the lattice level, we first investigate the nonlinear effective elastic properties without considering any magnetic field and compare the results with available literature. It provides a validation of the proposed nonlinear large deformation framework at the lattice level. After establishing adequate validation both at the beam level and lattice level, we demonstrate the on-demand modulation of effective elastic properties of the lattice metamaterial as a function of the magnetic field.

For beam level validation under magnetic field and mechanical load, we have compared the results obtained from the numerical model with those available in the literature individually for the two cases. Figure 4 shows that the results of the current analysis considering only mechanical load (and no external magnetic intensity) are close to those of reference literature, affirming the validity of the numerical model. Note that we have considered different magnitudes of loading and boundary conditions for this purpose, including the specific boundary condition necessary (one end fixed and the other end rotationally restrained, refer to figure 4(E)) for the lattice-level analysis. Figure 5 shows that the results of the current analysis considering only external magnetic intensity (and no mechanical load) are also in good agreement with those of reference literature, ascertaining the validity of the numerical model further (considering both deformation and rotational angles). Beam-level validations of the nonlinear deformation under both mechanical and magnetic loading ensure that the beam model is accurate enough for adopting it to the subsequent

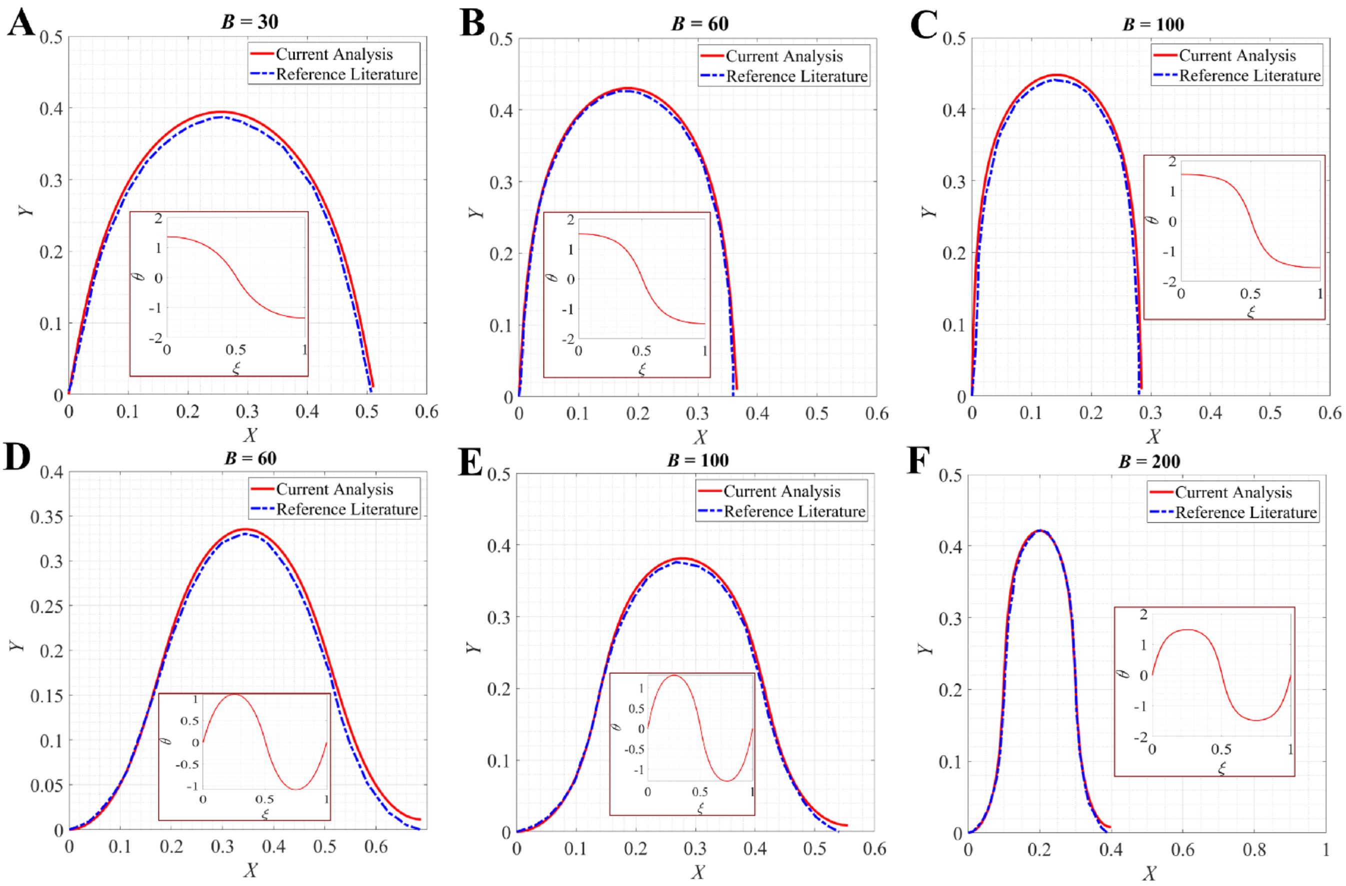

Figure 5. Numerical validation for a HMS beam element with only external magnetic flux density and no external mechanical load. (A) Comparison of the n-Shaped deformation of the HMS beam when $B = 30$ using the numerical model, with the reference literature [61]. (B) Comparison of the n-Shaped deformation of the HMS beam when $B = 60$ using the numerical model, with the reference literature [61]. (C) Comparison of the n-Shaped deformation of the HMS beam when $B = 100$ using the numerical model, with the reference literature [61]. (D) Comparison of the Ω-Shaped deformation of the HMS beam when $B = 60$ using the numerical model, with the reference literature [61]. (E) Comparison of the Ω-Shaped deformation of the HMS beam when $B = 100$ using the numerical model, with the reference literature [61]. (F) Comparison of the Ω-Shaped deformation of the HMS beam when $B = 200$ using the numerical model, with the reference literature [61]. The inset figures show the variation of rotation angle using the numerical model for each shape of deformation, obtained based on the current computational model.

lattice level analysis (note that the unit cell level mechanics here is primarily dependent on the beam level deformation, which we have extensively validated considering nonlinearity, mechanical load, magnetic field and appropriate boundary condition).

After having beam-level validations considering both mechanical load and magnetic field, we focus on lattice-level validation of the nonlinear elastic properties. Figure 6 presents the comparison of results for a hexagonal lattice using the results obtained from the proposed numerical model with those available in the literature. For all the nonlinear elastic properties, we find that the results match quite well for different values of far-field mechanical stress under the normal and shear modes. The numerical results converge to the widely accepted closed-form solutions [15] in case of small deformation. Thus, figures 4–6 validate the proposed numerical framework extensively at two levels, one at the beam level and the other at the lattice level, considering nonlinear large deformation under mechanical load and magnetic field. In the following paragraphs, we first investigate the nonlinear elastic properties of lattices without any magnetic field, followed by exploring the effect of magnetic field for active on-demand modulation of these effective elastic properties. The results are presented both for compressive and tensile far-field stresses separately (note that the shear modulus remains unaltered for clockwise and anti-clockwise directions).

Figures 7 and 8 investigate the nonlinear variation of five in-plane elastic moduli under large deformation due to only mechanical stresses (no external magnetic field). The results are presented considering both auxetic and non-auxetic microstructures considering different cell angles. The effect of beam-level axial deformation is studied by comparing the elastic moduli calculated based on only bending deformation and the combined effect of bending and axial deformation. Significant variation of the elastic moduli at higher values of applied far-field stresses affirms that it is necessary to incorporate the effect of nonlinearity due to the large deformation of beams and subsequent incremental change in the unit cell geometry. The Poisson's ratios are not affected by applied stress when only bending deformation is considered, while these

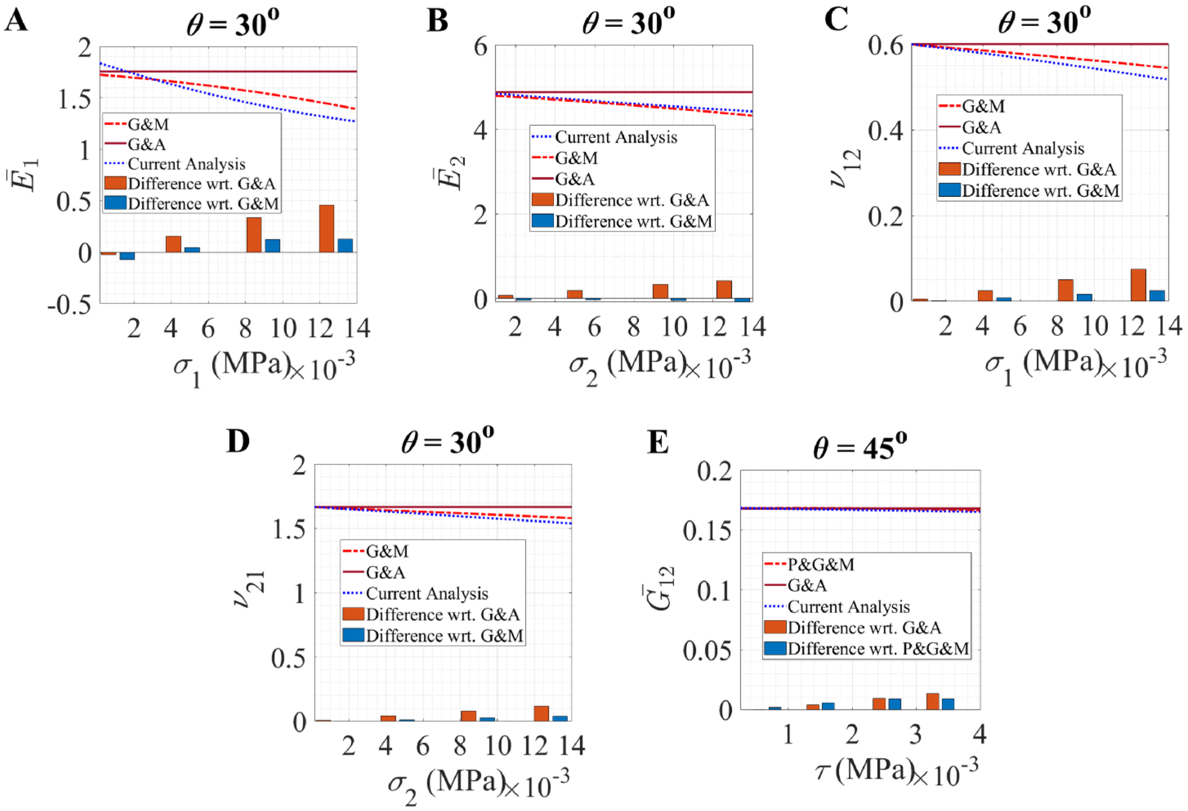

Figure 6. Numerical validation for nonlinear lattices with only mechanical load (compressive far-field lattice-level stress) and no external magnetic flux density. (A) Comparison of the non-dimensionalized nonlinear longitudinal Young's modulus $\bar{E}_1$ using the numerical model, with reference literature. (B) Comparison of the non-dimensionalized nonlinear transverse Young's modulus $\bar{E}_2$ using the numerical model, with reference literature. (C) Comparison of the nonlinear Poisson's ratio, ν_{12},using the numerical model with reference literature. (D) Comparison of the nonlinear Poisson's ratio, ν_{21}, using the numerical model with reference literature. (E) Comparison of the non-dimensionalized nonlinear transverse Shear Modulus $\bar{G}_{12}$ using the numerical model, with reference literature. The bar chart shown in the figures presents the difference of values when compared to the reference literature at different stress values. G&A refers to the reference literature [15], G&M refers to the reference literature [62] and P&G&M refers to the reference literature [65]. The cell angles considered in this analysis are based on the availability of results from literature.

become stress-dependent when the coupled effect of bending and axial deformations are accounted. In the following paragraphs, we would explore the influence of external magnetic fields in addition to the far-field mechanical stresses. The combined effect of transverse bending and axial deformation is considered (along with a comparative perspective of the scenario when only beam-level bending deformations are considered) at the beam level for evaluating the effective elastic properties of the lattices under the application of both far-field mechanical stresses and magnetic fields. Note that, for active effective elastic property modulation, we have applied the magnetic field only vertically as shown in figures 2 and 3. In this section, we will present the results considering two cases for better clarity in understanding the multi-physical behavior, one mechanical load dominated and the other magnetic field intensity B dominated. For the former case, we take comparatively lesser values of B (ranging from -0.1 to 0.1) and higher for the latter (ranging from -10 to 10). In all the analyses, geometric parameters h, $\frac{h}{l_s^0}$ and $\frac{t}{l_s^0}$ are considered as 3.67 mm, 2 and 10^{-2} respectively. Note that these microstructural parameters can also be varied (/designed) for expanding the range of active property modulation in future studies.

Figure 9 presents the variation in elastic moduli E_1, E_2 and G_{12} of hexagonal HMS lattices in mechanical load-dominated case with externally applied stress, considering both the bending and axial deformations at beam level. The right vertical axis of these plots presents the only bending deformation case, while the left vertical axis presents the combined bending and axial deformation. Note that the three elastic moduli are shown considering non-dimensional forms as E_1/E, E_2/E and G_{12}/E, where E represents the intrinsic equivalent Young's modulus of the constituting beam members making up the unit cell. From the figures, we find that initially the elastic moduli both for only bending and for bending and axial deformation case match with each other while they tend to differ with increasing applied stress values. This is because as the stress increases, the axial deformation component of the total deformation, which is initially very small also increases significantly. As the axial deformation increases, the elastic moduli decrease when compared to only the bending case (refer to equations (31), (39) and (51)). It may be noted that though the combined

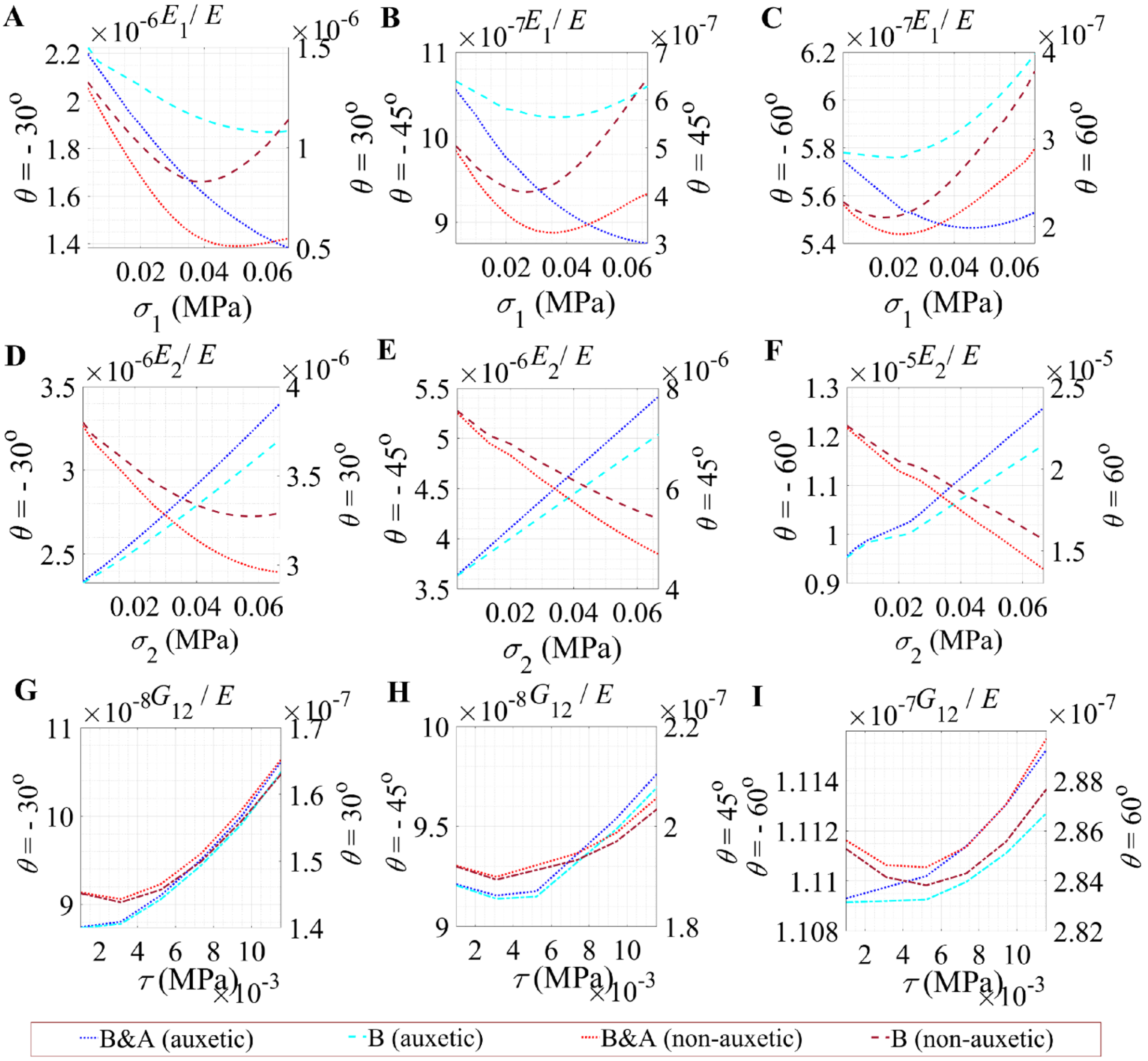

Figure 7. Variation of nonlinear Young's moduli and in-plane shear modulus for hexagonal lattices acted upon by mechanical load only (compressive far-field lattice-level stress). (A) Variation of non-dimensionalized longitudinal Young's modulus, E_1/E, with the compressive stress field, σ_1, for the auxetic case ($\theta = -30°$) on the left axis and for the non-auxetic case ($\theta = 30°$) on the right axis. (B) Variation of non-dimensionalized longitudinal Young's modulus, E_1/E, with the compressive stress field, σ_1, for the auxetic case ($\theta = -45°$) on the left axis and for the non-auxetic case ($\theta = 45°$) on the right axis. (C) Variation of non-dimensionalized longitudinal Young's modulus, E_1/E, with the compressive stress field, σ_1, for the auxetic case ($\theta = -60°$) on the left axis and for the non-auxetic case ($\theta = 60°$) on the right axis. (D) Variation of non-dimensionalized transverse Young's modulus, E_2/E, with the compressive stress field, σ_2, for the auxetic case ($\theta = -30°$) on the left axis and for the non-auxetic case ($\theta = 30°$) on the right axis. (E) Variation of non-dimensionalized transverse Young's modulus, E_2/E, with the compressive stress field, σ_2, for the auxetic case ($\theta = -45°$) on the left axis and for the non-auxetic case ($\theta = 45°$) on the right axis. (F) Variation of non-dimensionalized transverse Young's modulus, E_2/E, with the compressive stress field, σ_2, for the auxetic case ($\theta = -60°$) on the left axis and for the non-auxetic case ($\theta = 60°$) on the right axis. (G) Variation of non-dimensionalized shear modulus, G_{12}/E, with the shear stress field, τ, for the auxetic case ($\theta = -30°$) on the left axis and for the non-auxetic case ($\theta = 30°$) on the right axis. (H) Variation of non-dimensionalized Shear modulus, G_{12}/E, with the shear stress field, τ, for the auxetic case ($\theta = -45°$) on the left axis and for the non-auxetic case ($\theta = 45°$) on the right axis. (I) Variation of non-dimensionalized Shear modulus, G_{12}/E, with the shear stress field, τ, for the auxetic case ($\theta = -60°$) on the left axis and for the non-auxetic case ($\theta = 60°$) on the right axis. Here we have presented the results considering both bending and axial deformation and only bending deformation (B&A denotes the case considering both bending and axial deformations while B represents the case considering only bending deformation).

axial and bending deformation case is more complicated and computationally expensive, it provides more accurate results compared to the only bending deformation case. We notice from the figures (primarily based on the combined effect of axial and bending deformations) that, in general, for each non-auxetic orientation θ of the microstructure, the longitudinal elastic modulus decreases first and then begins to increase with increasing stress σ_1 values. Also as B decreases, E_1/E decreases, for each θ. For auxetic cases, the longitudinal elastic modulus decreases with increasing stress σ_1 values. As B decreases, E_1/E increases, for each θ. The transverse elastic modulus decreases for the non-auxetic cases while it increases

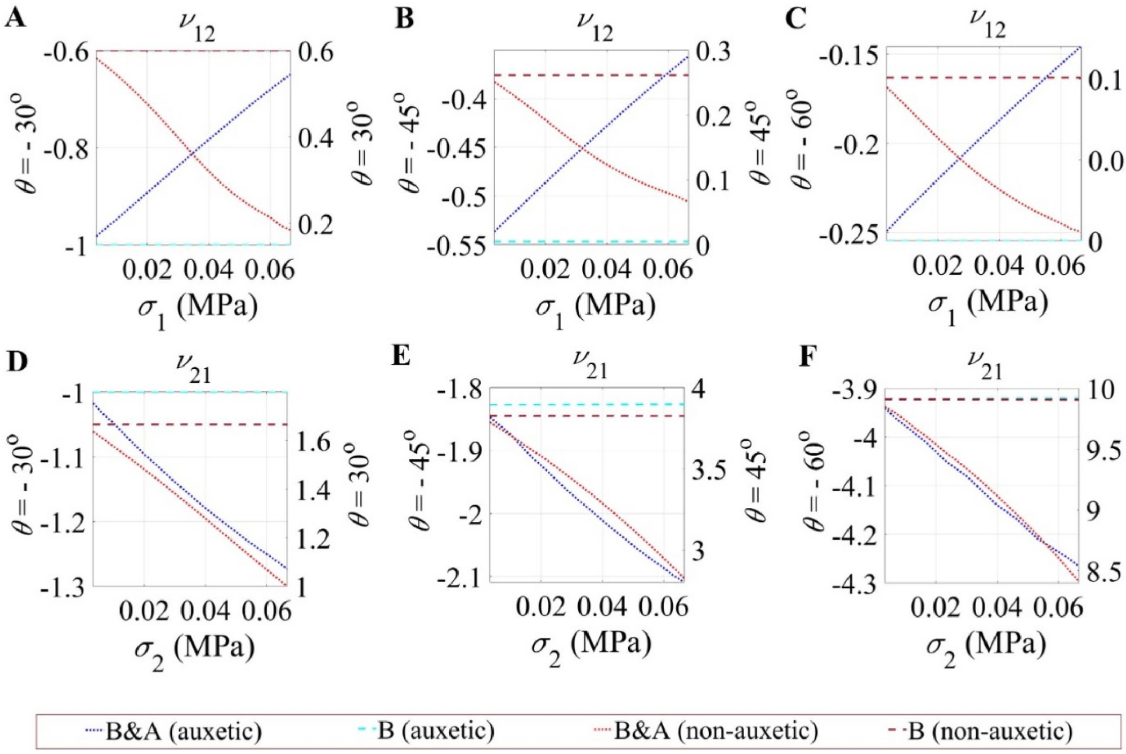

Figure 8. Variation of nonlinear Poisson's ratios for hexagonal lattices acted upon by mechanical load only (compressive far-field lattice-level stress). (A) Variation of longitudinal Poisson's ratio, ν_{12}, with the compressive stress field, σ_1, for the auxetic case ($\theta = -30^\circ$) on the left axis and for the non-auxetic case ($\theta = 30^\circ$) on the right axis. (B) Variation of longitudinal Poisson's ratio, ν_{12}, with the compressive stress field, σ_1, for the auxetic case ($\theta = -45^\circ$) on the left axis and for the non-auxetic case ($\theta = 45^\circ$) on the right axis. (C) Variation of longitudinal Poisson's ratio, ν_{12}, with the compressive stress field, σ_1, for the auxetic case ($\theta = -60^\circ$) on the left axis and for the non-auxetic case ($\theta = 60^\circ$) on the right axis. (D) Variation of transverse Poisson's ratio, ν_{21}, with the compressive stress field, σ_2, for the auxetic case ($\theta = -30^\circ$) on the left axis and for the non-auxetic case ($\theta = 30^\circ$) on the right axis. (E) Variation of transverse Poisson's ratio, ν_{21}, with the compressive stress field, σ_2, for the auxetic case ($\theta = -45^\circ$) on the left axis and for the non-auxetic case ($\theta = 45^\circ$) on the right axis. (F) Variation of transverse Poisson's ratio, ν_{21}, with the compressive stress field, σ_2, for the auxetic case ($\theta = -60^\circ$) on the left axis and for the non-auxetic case ($\theta = 60^\circ$) on the right axis. Here we have presented the results considering both bending and axial deformation and only bending deformation (B&A denotes the case considering both bending and axial deformations while B represents the case considering only bending deformation).

for the auxetic cases with increasing stress σ_2 values. Here as B decreases, E_2/E increases, for each θ. The in-plane shear modulus increases with increasing stress τ values. Also, in general, as B decreases, G_{12}/E, increases, for each θ.

Figure 10 presents the variation in Poisson's ratios ν_{12} and ν_{21} of hexagonal HMS lattices in the mechanical load-dominated case with externally applied stress, considering both the bending and axial deformations. Here we have not presented the only bending deformation case because for this case the Poisson's ratios are independent of the external stresses and magnetic field intensity. They depend only on the geometric configurations as evident from the expressions in equations (52*b*) and (52*d*). From the figures, we notice that for each microstructural non-auxetic orientation θ, the Poisson's ratio, ν_{12} decreases with increasing stress σ_1 values. In auxetic case, for each θ, the Poisson's ratio, ν_{12} increases with increasing stress σ_1 values. Also as B decreases, ν_{12} decreases, for each θ, both in auxetic and non-auxetic cases. The transverse Poisson's ratio, ν_{21} decreases with increasing stress σ_2 values. With decrease in B, ν_{21} increases, for each θ, both in auxetic and non-auxetic cases.

Figure 11 presents the variation in elastic moduli E_1, E_2 and G_{12} of hexagonal HMS lattices in the magnetic field intensity-dominated case with externally applied stress, considering both the bending and axial deformations. The right vertical axis of these plots presents the only bending deformation case, while the left vertical axis presents the combined bending and axial deformation. Note that the three elastic moduli are shown considering non-dimensional forms as E_1/E, E_2/E and G_{12}/E, where E represents the intrinsic equivalent Young's modulus of the constituting beam members making up the unit cell. From the figures, we find that the elastic moduli both for only bending and for bending and axial deformation case follow a similar trend though their values differ with increasing applied stress values. This is because of the fact that as the stress increases, the axial deformation component of the total deformation becomes dominant. As the axial deformation increases, the elastic moduli decrease when compared to only bending case (refer to equations (31), (39) and (51)). The results show that a wide range of effective elastic moduli (including positive and negative values) can be achieved with their active programmable feature based on the coupled

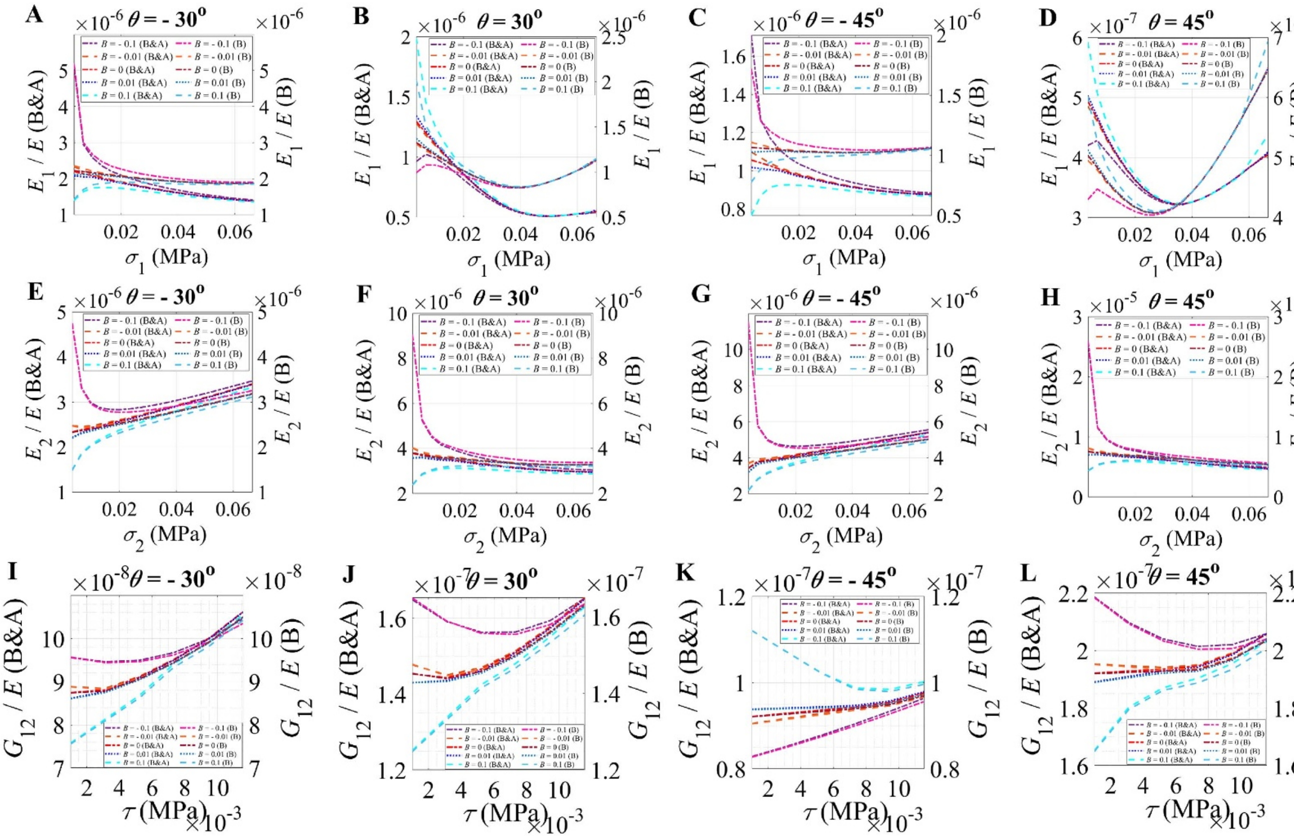

Figure 9. Variation of nonlinear elastic moduli for hexagonal lattices, considering both bending and axial deformations for mechanical load dominated case (compressive far-field lattice-level stress). (A) Variation of non-dimensionalized longitudinal Young's modulus, E_1/E, with the compressive stress field, σ_1, at different values of external magnetic field intensity B for $\theta = -30°$. (B) Variation of non-dimensionalized longitudinal Young's modulus, E_1/E, with the compressive stress field, σ_1, at different values of external magnetic field intensity B for $\theta = 30°$. (C) Variation of non-dimensionalized longitudinal Young's modulus, E_1/E, with the compressive stress field, σ_1, at different values of external magnetic field intensity B for $\theta = -45°$. (D) Variation of non-dimensionalized longitudinal Young's modulus, E_1/E, with the compressive stress field, σ_1, at different values of external magnetic field intensity B for $\theta = 45°$. (E) Variation of non-dimensionalized transverse Young's modulus, E_2/E, with the compressive stress field, σ_2, at different values of external magnetic field intensity B for $\theta = -30°$. (F) Variation of non-dimensionalized transverse Young's modulus, E_2/E, with the compressive stress field, σ_2, at different values of external magnetic field intensity B for $\theta = 30°$. (G) Variation of non-dimensionalized transverse Young's modulus, E_2/E, with the compressive stress field, σ_2, at different values of external magnetic field intensity B for $\theta = -45°$. (H) Variation of non-dimensionalized transverse Young's modulus, E_2/E, with the compressive stress field, σ_2, at different values of external magnetic field intensity B for $\theta = 45°$. (I) Variation of non-dimensionalized Shear modulus, G_{12}/E, with the shear stress field, τ, at different values of external magnetic field intensity B for $\theta = -30°$. (J) Variation of non-dimensionalized Shear modulus, G_{12}/E, with the shear stress field, τ, at different values of external magnetic field intensity B for $\theta = 30°$. (K) Variation of non-dimensionalized shear modulus, G_{12}/E, with the shear stress field, τ, at different values of external magnetic field intensity B for $\theta = -45°$. (L) Variation of non-dimensionalized shear modulus, G_{12}/E, with the shear stress field, τ, at different values of external magnetic field intensity B for $\theta = 45°$. Here B&A on the left axes of the plots denotes the case considering both bending and axial deformations and B on the right axes of the plots represents the case considering only bending deformation.

effect of applied stress and magnetic field. It may be noted that though the combined axial and bending deformation case is more complicated and computationally expensive, it provides more accurate results compared to the only bending deformation case. We notice from the figures (primarily based on the combined effect of axial and bending deformations) that for each microstructural orientation θ, the longitudinal and transverse elastic modulus either increase or decrease with increasing stress σ_1 values, depending on the values of B. The nature and values of the effective elastic moduli depend on the relative influence of mechanical stress and magnetic field on the beam-level deformations. If they are opposite in nature, the combined effect may lead to negative values of effective elastic moduli. Further, other extreme values (very high and very low) can also be realized actively by exploiting such coupled influences. The in-plane shear modulus shows an increasing trend with increasing stress τ values as a general trend.

Figure 12 presents the variation in Poisson's ratios ν_{12} and ν_{21} of hexagonal HMS lattices in the magnetic field intensity-dominated case with externally applied stress, considering both the bending and axial deformations. Here we have not presented the only bending deformation case because for this case the Poisson's ratios are independent of the external stresses and magnetic field intensity. They depend only on the geometric configurations as evident from the expressions in equations (52*b*) and (52*d*). From the figures, we notice that

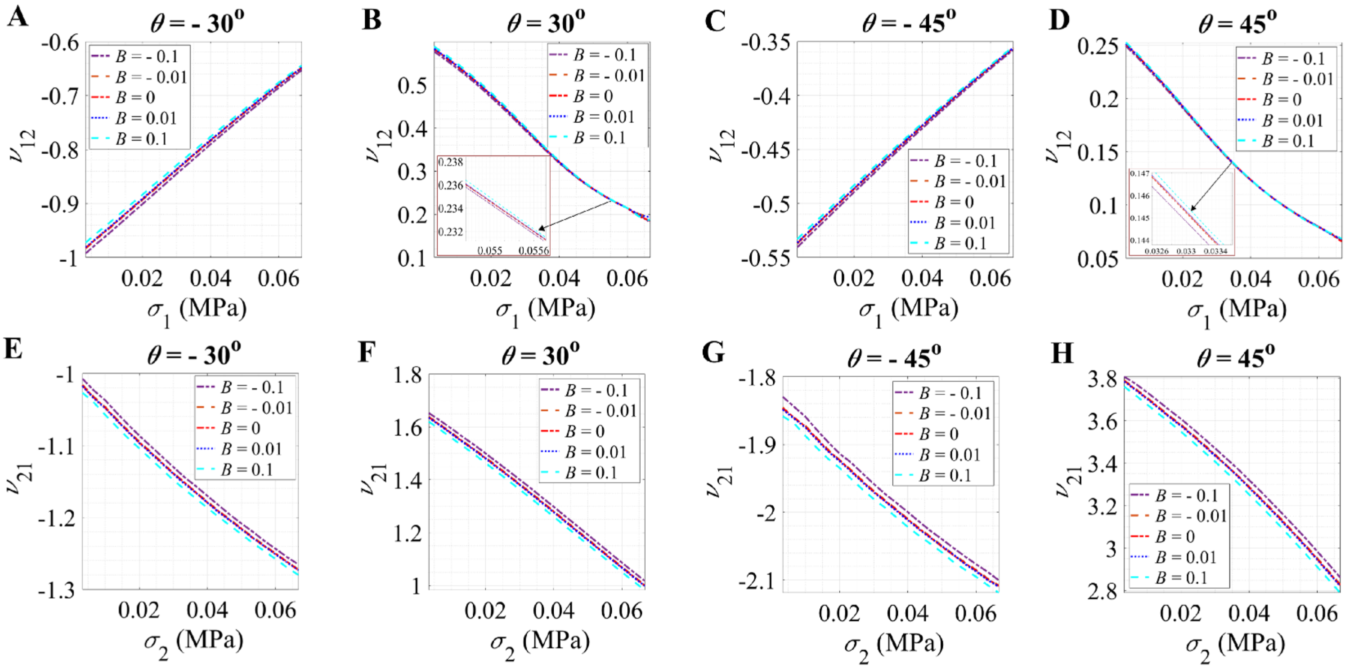

Figure 10. Variation of nonlinear Poisson's ratios for hexagonal lattices, considering both bending and axial deformations for mechanical load dominated case (compressive far-field lattice-level stress). (A) Variation of Poisson's ratio ν_{12} with the compressive stress field, σ_1, at different values of external magnetic field intensity B for $\theta = -30°$. (B) Variation of Poisson's ratio ν_{12} with the compressive stress field, σ_1, at different values of external magnetic field intensity B for $\theta = 30°$. (C) Variation of Poisson's ratio ν_{12} with the compressive stress field, σ_1, at different values of external magnetic field intensity B for $\theta = -45°$. (D) Variation of Poisson's ratio ν_{12} with the compressive stress field, σ_1, at different values of external magnetic field intensity B for $\theta = 45°$. (E) Variation of Poisson's ratio ν_{21} with the compressive stress field, σ_2, at different values of external magnetic field intensity B for $\theta = -30°$. (F) Variation of Poisson's ratio ν_{21} with the compressive stress field, σ_2, at different values of external magnetic field intensity B for $\theta = 30°$. (G) Variation of Poisson's ratio ν_{21} with the compressive stress field, σ_2, at different values of external magnetic field intensity B for $\theta = -45°$. (H) Variation of Poisson's ratio ν_{21} with the compressive stress field, σ_2, at different values of external magnetic field intensity B for $\theta = 45°$.

for each microstructural orientation θ, the Poisson's ratio, ν_{12} shows a varying trend with increasing stress σ_1 values based on the value of B. It either increases or decreases with stress based on the beam-level deflections which in turn are influenced by the combined effect of both mechanical load and B values. The transverse Poisson's ratio, ν_{21} decreases with increasing stress σ_2 values. With decrease in B, ν_{21} increases, for each θ, both in auxetic and non-auxetic cases.

Note that the above discussed results (all figures concerning elastic moduli and Poisson's ratio's presented in the main paper) correspond to the external far-field stresses that are compressive in nature. The results with the hexagonal lattice being subjected to tensile external far-field stresses are presented in the supplementary document. In this paragraph and the subsequent ones, we will discuss the same. We have referred to the figures in supplementary document with a prefix S. Figure S1 presents the comparison of results for a hexagonal lattice using the results obtained from the proposed numerical model with those available in the literature. Since the lattice is subjected to far-field tensile stress, the validation and subsequent results are presented for the four in-plane elastic moduli (E_1, E_2, ν_{12} and ν_{21}) . For all these nonlinear elastic properties, we find that the results show good agreement with literature [62] for different values of far-field mechanical stress. The numerical results converge to the widely accepted closed-form solutions [15] in case of small deformation.

Figures S2 and S3 investigate the nonlinear variation of the four in-plane elastic moduli, as mentioned above, under large deformation due to only mechanical tensile stresses with no external magnetic field, considering different cell angles. The effect of beam-level axial deformation is studied by comparing the elastic moduli calculated based on only bending deformation and the combined effect of bending and axial deformation. Here we observe significant variation of the elastic moduli at higher values of applied far-field tensile stresses which reaffirms the necessity of incorporating the effect of nonlinearity due to the large deformation of beams and subsequent incremental change in the unit cell geometry. The Poisson's ratios are not affected by applied stress when only bending deformation is considered, while these become stress-dependent when the coupled effect of bending and axial deformations are accounted. Note that the lattice properties for the tensile case are same as that of the compressive one.

Figure S4 presents the variation in elastic moduli E_1, E_2 and G_{12} of hexagonal HMS lattices in mechanical load-dominated case with externally applied tensile stress, considering both the bending and axial deformations at beam level. The right vertical axis of these plots presents the only bending deformation case, while the left vertical axis presents the combined bending and axial deformation. Note that the two elastic moduli are shown considering non-dimensional forms as E_1/E and E_2/E, where E represents the intrinsic equivalent Young's modulus

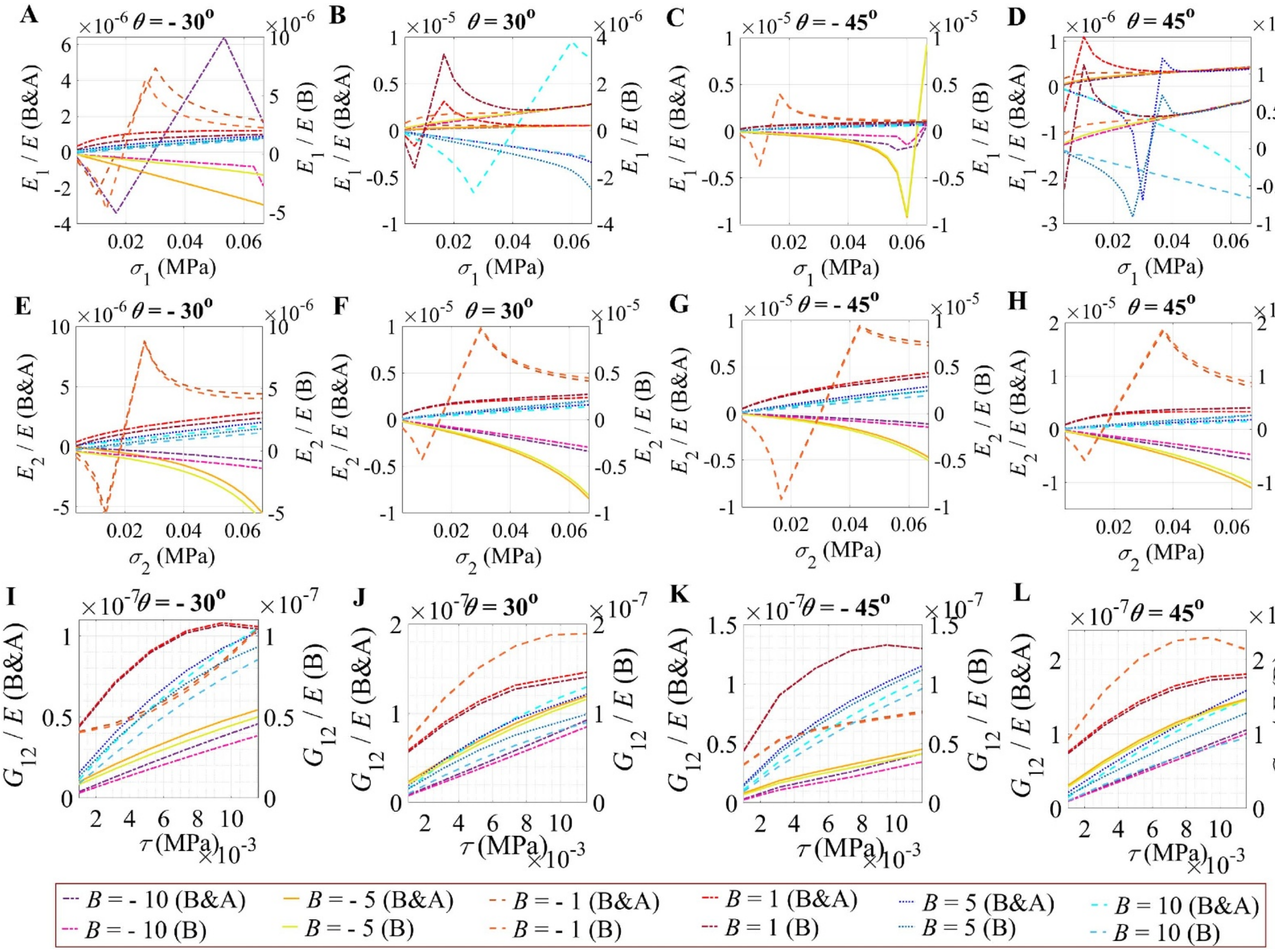

Figure 11. Variation of nonlinear elastic moduli for hexagonal lattices, considering both bending and axial deformations for magnetic intensity dominated case (compressive far-field lattice-level stress). (A) Variation of non-dimensionalized longitudinal Young's modulus, E_1/E, with the compressive stress field, σ_1, at different values of external magnetic field intensity B for $\theta = -30°$. (B) Variation of non-dimensionalized longitudinal Young's modulus, E_1/E, with the compressive stress field, σ_1, at different values of external magnetic field intensity B for $\theta = 30°$. (C) Variation of non-dimensionalized longitudinal Young's modulus, E_1/E, with the compressive stress field, σ_1, at different values of external magnetic field intensity B for $\theta = -45°$. (D) Variation of non-dimensionalized longitudinal Young's modulus, E_1/E, with the compressive stress field, σ_1, at different values of external magnetic field intensity B for $\theta = 45°$. (E) Variation of non-dimensionalized transverse Young's modulus, E_2/E, with the compressive stress field, σ_2, at different values of external magnetic field intensity B for $\theta = -30°$. (F) Variation of non-dimensionalized transverse Young's modulus, E_2/E, with the compressive stress field, σ_2, at different values of external magnetic field intensity B for $\theta = 30°$. (G) Variation of non-dimensionalized transverse Young's modulus, E_2/E, with the compressive stress field, σ_2, at different values of external magnetic field intensity B for $\theta = -45°$. (H) Variation of non-dimensionalized transverse Young's modulus, E_2/E, with the compressive stress field, σ_2, at different values of external magnetic field intensity B for $\theta = 45°$. (I) Variation of non-dimensionalized shear modulus, G_{12}/E, with the shear stress field, τ, at different values of external magnetic field intensity B for $\theta = -30°$. (J) Variation of non-dimensionalized Shear modulus, G_{12}/E, with the shear stress field, τ, at different values of external magnetic field intensity B for $\theta = 30°$. (K) Variation of non-dimensionalized Shear modulus, G_{12}/E, with the shear stress field, τ, at different values of external magnetic field intensity B for $\theta = -45°$. (L) Variation of non- dimensionalized Shear modulus, G_{12}/E, with the shear stress field, τ, at different values of external magnetic field intensity B for $\theta = 45°$. Here B&A on the left axes of the plots denotes the case considering both bending and axial deformations and B on the right axes of the plots represents the case considering only bending deformation.

of the constituting beam members making up the unit cell. From the figures, we find that initially the elastic moduli both for only bending and for bending and axial deformation case match with each other while they tend to differ with increasing applied stress values. This is because as the stress increases, the axial deformation component of the total deformation, which is initially very small also increases significantly. Since the formulation of elastic moduli for the tensile case is similar to that of the compressive case (refer to equations (31), (39) and (51)), we observe that as the axial deformation increases, the elastic moduli decrease when compared to only the bending case. We notice from the figures (primarily based on the combined effect of axial and bending deformations) that for each non-auxetic orientation θ and broadly for all auxetic configuration of the microstructure, the longitudinal elastic modulus increases with increasing stress σ_1 values. Also, for the non-auxetic case, as B decreases, E_1/E increases, for each θ. For the auxetic case, as B decreases, E_1/E decreases, for each

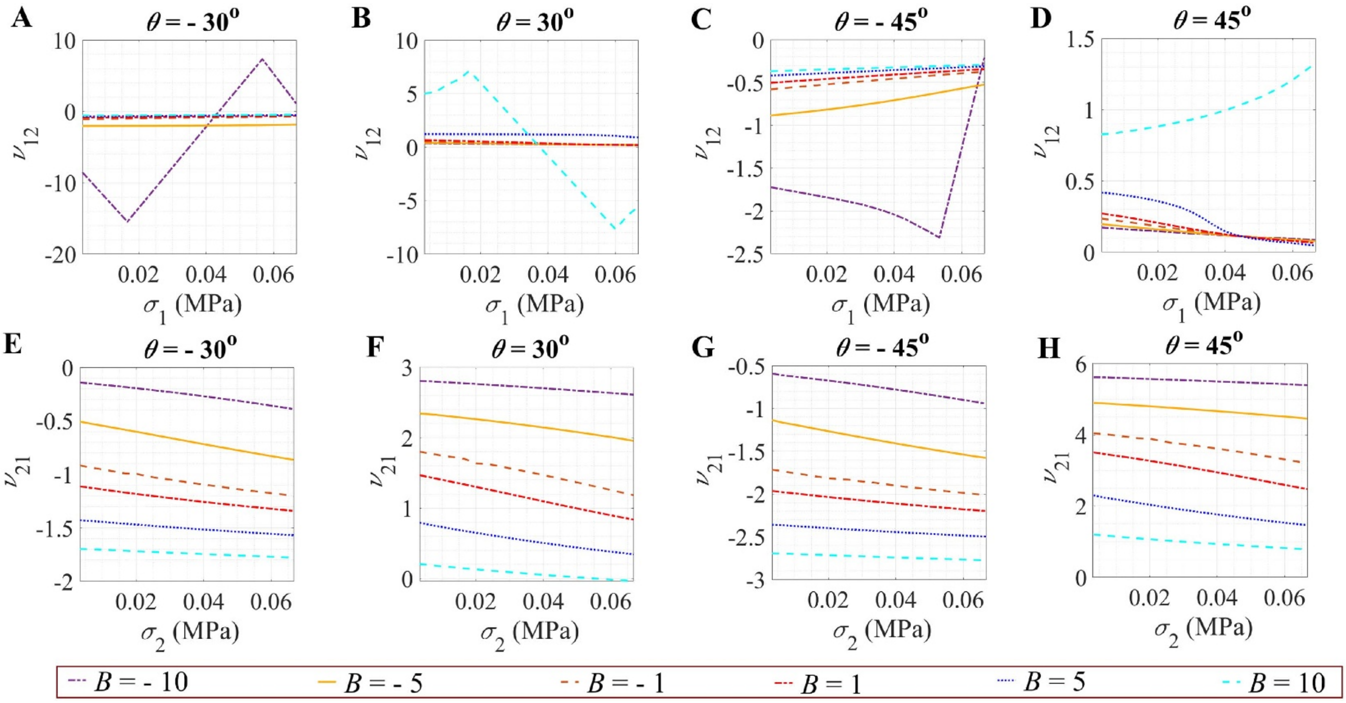

Figure 12. Variation of nonlinear Poisson's ratios for hexagonal lattices, considering both bending and axial deformations for magnetic intensity dominated case (compressive far-field lattice-level stress). (A) Variation of Poisson's ratio ν_{12} with the compressive stress field, σ_1, at different values of external magnetic field intensity B for $\theta = -30°$. (B) Variation of Poisson's ratio ν_{12} with the compressive stress field, σ_1, at different values of external magnetic field intensity B for $\theta = 30°$. (C) Variation of Poisson's ratio ν_{12} with the compressive stress field, σ_1, at different values of external magnetic field intensity B for $\theta = -45°$. (D) Variation of Poisson's ratio ν_{12} with the compressive stress field, σ_1, at different values of external magnetic field intensity B for $\theta = 45°$. (E) Variation of Poisson's ratio ν_{21} with the compressive stress field, σ_2, at different values of external magnetic field intensity B for $\theta = -30°$. (F) Variation of Poisson's ratio ν_{21} with the compressive stress field, σ_2, at different values of external magnetic field intensity B for $\theta = 30°$. (G) Variation of Poisson's ratio ν_{21} with the compressive stress field, σ_2, at different values of external magnetic field intensity B for $\theta = -45°$. (H) Variation of Poisson's ratio ν_{21} with the compressive stress field, σ_2, at different values of external magnetic field intensity B for $\theta = 45°$.

θ. The transverse elastic modulus increases for the non-auxetic cases while it decreases for the auxteic cases with increasing stress σ_2 values. Here as B decreases, E_2/E decreases, for each θ.

Figure S5 presents the variation in Poisson's ratios ν_{12} and ν_{21} of hexagonal HMS lattices in the mechanical load-dominated case with externally applied tensile stress, considering both the bending and axial deformations. Here we have not presented the only bending deformation case because for this case the Poisson's ratios are independent of the external stresses and magnetic field intensity and are dependent only on the geometric configurations. From the figures, we notice that for each microstructural non-auxetic orientation θ, the Poisson's ratio, ν_{12} increases with increasing stress σ_1 values. In auxetic case, for each θ, the Poisson's ratio, ν_{12} decreases with increasing stress σ_1 values. Also as B decreases, ν_{12} decreases, for each θ, both in auxetic and non-auxetic cases. The transverse Poisson's ratio, ν_{21} increases with increasing stress σ_2 values. With decrease in B, ν_{21} increases, for each θ, both in auxetic and non-auxetic cases.

Figure S6 presents the variation in elastic moduli E_1, E_2 and G_{12} of hexagonal HMS lattices in the magnetic field intensity-dominated case with externally applied tensile stress, considering both the bending and axial deformations. The right vertical axis of these plots presents the only bending deformation case, while the left vertical axis presents the combined bending and axial deformation. Note that the two elastic moduli are shown considering non-dimensional forms as E_1/E and E_2/E, where E represents the intrinsic equivalent Young's modulus of the constituting beam members making up the unit cell. From the figures, we find that the elastic moduli both for only bending and for bending and axial deformation case follow a similar trend though their values differ with increasing applied stress values. This is because of the fact that as the stress increases, the axial deformation component of the total deformation becomes dominant. Also, as the axial deformation increases, the elastic moduli decrease when compared to only bending case. The results show that a wide range of effective elastic moduli (including positive and negative values) can be achieved with their active programmable feature based on the coupled effect of applied stress and magnetic field. It may be noted that though the combined axial and bending deformation case is more complicated and computationally expensive, it provides more accurate results compared to the only bending deformation case. We notice from the figures (primarily based on the combined effect of axial and bending deformations) that for each microstructural orientation θ, the elastic moduli either increase or decrease with increasing stress σ_1 values, depending on the values of B. The nature and values of the effective elastic moduli depend on the relative influence of mechanical stress and magnetic field on the beam-level deformations. If they are opposite in nature, the combined effect may lead to negative values of effective elastic moduli. Further, other extreme values (very high and very low) can also be realized actively by exploiting such coupled influences.

Figure S7 presents the variation in Poisson's ratios ν_{12} and ν_{21} of hexagonal HMS lattices in the magnetic field intensity-dominated case with externally applied tensile stress, considering both the bending and axial deformations. Here we have not presented the only bending deformation case because for this case the Poisson's ratios are independent of the external stresses and magnetic field intensity and are dependent only on the geometric configurations. From the figures, we notice that for each microstructural orientation θ, the Poisson's ratio, ν_{12} shows a varying trend with increasing stress σ_1 values based on the value of B. It either increases or decreases with stress based on the beam-level deflections which in turn are influenced by the combined effect of both mechanical load and B values. The transverse Poisson's ratio, ν_{21} increases with increasing stress σ_2 values. With decrease in B, ν_{21} increases, for each θ, both in auxetic and non-auxetic cases.

The numerical results presented in this section demonstrate that the nonlinear Young's moduli, shear modulus and Poisson's ratios can be actively modulated as a function of externally applied far-field mechanical stress (tensile and compressive) and magnetic field. It can be noticed that the trends of nonlinear variations of elastic moduli differ significantly in the mechanical stress dominated and magnetic intensity dominated cases, as presented in figures 9–12. The extent of such modulation can further be controlled by microstructural design parameters such as cell angles, length and thickness of the cell walls, and intrinsic material properties. We note that it is possible to achieve a wide range of variation in the elastic properties in an on-demand and contactless paradigm including active transition between negative and positive values of the elastic moduli and Poisson's ratios. Effective elastic moduli being one of the fundamental properties of a material, the capability of having active control through a contactless framework would essentially lead to on-demand programming of a range of static and dynamic structural behavior, including direction-dependent deformation, vibration, wave propagation and control, impact and penetration resistance, energy absorption, shape morphing, robotic motion and actuation.

In this paper, we have focused on the hexagonal lattices with auxetic and non-auxetic configurations. It is primarily because the hexagonal lattice-based forms are widely encountered in naturally occurring and artificial structures across the macro, micro and even nanoscales (like graphene and hBN nanostructures, woods and bones microstructures and sandwich structures' core) [15, 33, 66]. Due to their high specific strength and stiffness along with high energy absorption capability and crushing resistance, and at the same time being lightweight, these hexagonal lattices have a wide range of structural and industrial applications [67, 68]. Though the present study is confined only to hexagonal lattices, the developed semi-analytical framework is directly applicable to various other 2D lattice forms such as rhombic and rectangular (by considering special cases of having the vertical cell wall length and cell angles as zero, respectively). A range of other active 2D and 3D periodic lattices can also be analyzed based on the proposed framework by considering appropriate unit cells. The current focus of this paper is effective elastic moduli and their active control that would essentially affect the stiffness. However, other mechanical properties of lattices such as failure strength [69] can also be controlled actively following a similar framework considering beam-level bending and axial deformations as proposed here.

It may be noted that the focus of this work is theoretical development of the computational framework and proposition of the concept of contactless active modulation of effective elastic properties. However, future research will follow the prospective manufacturing of the proposed lattices. With the recent advancements in 3D and 4D printing (/additive manufacturing) [70–73], it is possible to fabricate complex lattice structures along with the inclusion of magnetoactive particles.

4. Conclusions and perspective

With the quest of achieving contactless on-demand modulation of effective elastic properties, we propose a new class of lattice materials in this article wherein the beam-level multi-physical deformation behavior can be exploited as a function of external magnetic field by considering HMS beams. A semi-analytical bottom-up multi-level approach is developed for evaluating the active nonlinear elastic properties of the lattices under large deformation. In the first stage, we have developed a computational framework for analyzing the multi-physical nonlinear deformation behavior of HMS beams under the combined application of mechanical load and magnetic field. Subsequently, the beam-level deformation behavior is integrated with unit cell-based mechanics of lattices for obtaining the effective elastic properties of lattice materials in an efficient semi-analytical framework.

Before demonstrating the active modulation of elastic properties, the developed computational framework is validated extensively both at the beam level and lattice level considering different boundary conditions, nonlinearity mechanical loading and magnetic fields. The numerical results are systematically presented first exploring the nonlinear effective elastic moduli under only far-field mechanical stresses, followed by investigating the coupled influence of external mechanical stresses and magnetic fields. For investigating the coupled influence with more clarity, we have adopted two different possible scenarios of mechanical load dominated case and magnetic field dominated case depending on the relative intensity of applied far-field stress and magnetic field. The results demonstrate that the nonlinear Young's moduli, shear modulus and Poisson's ratios can be actively modulated as a function of externally applied far-field mechanical stress and magnetic field within a broadband of respective values. The extent of such modulation can further be controlled by microstructural design parameters such as cell angles, length and thickness of the cell walls, and intrinsic material properties. It is possible to achieve an active transition between negative and positive values of the elastic moduli and Poisson's ratios. More interestingly, the active programming of effective elastic properties at the lattice level can be achieved in a contactless arrangement without the necessity of having a complex network of electrical circuits embedded within the microstructure as in the case of piezoelectric lattices.

In general, tremendous progress in the field of lattice-based metamaterials has led to the current capabilities where it is possible to have a wide range of effective mechanical properties based on their designed microstructural geometry in a passive framework, meaning it is not possible to actively modulate the lattice-level properties after they are manufactured. Thus the on-demand control of mechanical properties is lacking, which is crucial for a range of multi-functional applications in advanced structural and mechanical systems. The current development concerning active lattices addresses this issue with the additional advantage of contactless nonlinear modulation. By externally applying different values of the magnetic field intensity, we can get different elastic properties, and that too from a distance. Essentially, this will help in optimizing the material utilization to an extreme extent by controlling the stiffness of a structure based on operational demands. For example, the stiffness of a structure can be actively increased during an operational condition when higher magnitudes of loads are experienced to keep the deformations under control or the natural frequencies need to be increased to avoid resonance under dynamic loading. The stiffness can also be actively reduced to allow large deformation and shape control for (soft-)robotic motions or increased energy absorption and avert sudden failure. The numerical results in this paper show that the effective properties can be actively programmed as a function of the magnetic field covering a wide range (including programmable state transition with on-demand positive and negative values), leading to the behavior of soft polymer to stiff metals in a single lattice microstructure according to operational demands. Effective elastic moduli being one of the fundamental properties of a material, the capability of having active control would essentially lead to on-demand programming of a range of static and dynamic structural behavior, including direction-dependent deformation, vibration, wave propagation and control, impact and penetration resistance, energy absorption, shape morphing, robotic motion and actuation.

Data availability statement

All data that support the findings of this study are included within the article (and any supplementary files).

Acknowledgments

P S acknowledges the financial support from the Ministry of Education, India through a doctoral scholarship. T M would like to acknowledge the Initiation grant received from IIT Kanpur. The authors would also like to acknowledge the contribution of Deepak Ganesh (visiting student under SURGE internship program at IIT Kanpur) during the initial development of HMS beams.

Conflict of interest

The authors declare that they have no known competing financial interests or personal relationships that could have appeared to influence the work reported in this paper.

ORCID iD

T Mukhopadhyay https://orcid.org/0000-0002-0778-6515

References

[1] Mukhopadhyay T, Ma J, Feng H, Hou D, Gattas J M, Chen Y and You Z 2020 Programmable stiffness and shape modulation in origami materials: emergence of a distant actuation feature *Appl. Mater. Today* **19** 100537
[2] Kolken H M A and Zadpoor A A 2017 Auxetic mechanical metamaterials *RSC Adv.* **7** 5111–29
[3] Fleck N A, Deshpande V S and Ashby M F 2010 Micro-architectured materials: past, present and future *Proc. R. Soc.* A **466** 2495–516
[4] Lai Y, Wu Y, Sheng P and Zhang Z Q 2011 Hybrid elastic solids *Nat. Mater.* **10** 620–4
[5] Liang Y, Lin H, Lin S, Wu J, Li W, Meng F, Yang Y, Huang X, Jia B and Kivshar Y 2021 Hybrid anisotropic plasmonic metasurfaces with multiple resonances of focused light beams *Nano Lett.* **21** 8917–23
[6] Tang Y, Liang Y, Yao J, Chen M K, Lin S, Wang Z, Zhang J, Huang X G, Yu C and Tsai D P 2023 Chiral bound states in the continuum in plasmonic metasurfaces *Laser Photon. Rev.* 2200597
[7] Karlicic D, Cajic M, Chatterjee T and Adhikari S 2021 Wave propagation in mass embedded and pre-stressed hexagonal lattices *Compos. Struct.* **256** 113087
[8] Harris J and McShane G 2020 Metallic stacked origami cellular materials: additive manufacturing, properties and modelling *Int. J. Solids Struct.* **185–186** 448–66
[9] Cummer S A, Christensen J and Alù A 2016 Controlling sound with acoustic metamaterials *Nat. Rev. Mater.* **1** 16001
[10] Ouyang H, Gu Y, Gao Z, Hu L, Zhang Z, Ren J, Li B, Sun J, Chen Y and Ding X 2023 Kirigami-inspired thermal regulator *Phys. Rev. Appl.* **19** L011001
[11] Galea R, Dudek K K, Farrugia P-S, Zammit Mangion L, Grima J N and Gatt R 2022 Reconfigurable magneto-mechanical metamaterials guided by magnetic fields *Compos. Struct.* **280** 114921
[12] Lim T-C 2017 Analogies across auxetic models based on deformation mechanism *Phys. Status Solidi* **11** 1600440
[13] Pirhaji A, Jebellat E, Roudbarian N, Mohammadi K, Movahhedy M R and Asle Zaeem M 2022 Large deformation of shape-memory polymer-based lattice metamaterials *Int. J. Mech. Sci.* **232** 107593
[14] Mukhopadhyay T, Adhikari S and Alu A 2019 Theoretical limits for negative elastic moduli in subacoustic lattice materials *Phys. Rev.* B **99** 094108
[15] Gibson L and Ashby M F 1999 *Cellular Solids Structure and Properties* (Cambridge: Cambridge University Press)
[16] Singh A, Mukhopadhyay T, Adhikari S and Bhattacharya B 2022 Extreme on-demand contactless modulation of elastic properties in magnetostrictive lattices *Smart Mater. Struct.* **31** 125005

[17] Garcia-Taormina A R, Alwen A, Schwaiger R and Hodge A M 2021 A review of coated nano-and micro-lattice materials *J. Mater. Res.* **36** 3607–27

[18] Mizzi L, Attard D, Gatt R, Dudek K K, Ellul B and Grima J N 2021 Implementation of periodic boundary conditions for loading of mechanical metamaterials and other complex geometric microstructures using finite element analysis *Eng. Comput.* **37** 1765–79

[19] Dey S and Karmakar A 2012 Free vibration analyses of multiple delaminated angle-ply composite conical shells—a finite element approach *Compos. Struct.* **94** 2188–96

[20] Garg A, Belarbi M-O, Chalak H and Chakrabarti A 2021 A review of the analysis of sandwich fgm structures *Compos. Struct.* **258** 113427

[21] Chakrabarti A, Sheikh A, Griffith M and Oehlers D 2012 Analysis of composite beams with partial shear interactions using a higher order beam theory *Eng. Struct.* **36** 283–91

[22] Sorohan S, Constantinescu D M, Sandu M and Sandu A G 2019 In-plane homogenization of commercial hexagonal honeycombs considering the cell wall curvature and adhesive layer influence *Int. J. Solids Struct.* **156–157** 87–106

[23] Isanaka B, Mukhopadhyay T, Varma R and Kushvaha V 2022 On exploiting machine learning for failure pattern driven strength enhancement of honeycomb lattices *Acta Mater.* **239** 118226

[24] Yongquiang L and Zhiquiang J 2008 Free flexural vibration analysis of symmetric rectangular honeycomb panels with SCSC edge supports *Compos. Struct.* **83** 154–8

[25] Mukhopadhyay T and Adhikari S 2016 Free vibration analysis of sandwich panels with randomly irregular honeycomb core *J. Eng. Mech.* **142** 06016008

[26] Zenkert D 1995 *An Introduction to Sandwich Construction* (Cradley Heath, Warley: Engineering Materials Advisory Services)

[27] Tornabene F, Viscoti M, Dimitri R and Aiello M A 2021 Higher order formulations for doubly-curved shell structures with a honeycomb core *Thin-Walled Struct.* **164** 107789

[28] Kundu D, Ghuku S, Naskar S and Mukhopadhyay T 2022 Extreme specific stiffness through interactive cellular networks in bi-level micro-topology architected metamaterials *Adv. Eng. Mater.* 2201407

[29] Tiwari P, Naskar S and Mukhopadhyay T 2023 Programmed out-of-plane curvature to enhance multimodal stiffness of bending-dominated composite lattices *AIAA J.* 1–19

[30] Mukhopadhyay T, Mahata A, Adhikari S and Zaeem M A 2017 Effective elastic properties of two dimensional multiplanar hexagonal nano-structures *2D Mater.* **4** 029501

[31] Chen J, Zhang X, Ying C, Ma H, Li J, Wang F and Guo H 2020 The influence of vacancy defects on elastic and electronic properties of tasi (5/3) desilicides from a first-principles calculations *Ceram. Int.* **46** 10992–9

[32] Chen J, Zhang X, Yang L and Wang F 2021 The vacancy defects and oxygen atoms occupation effects on mechanical and electronic properties of Mo_5Si_3 silicides *Commun. Theor. Phys.* **73** 045702

[33] Mukhopadhyay T and Adhikari S 2017 Effective in-plane elastic moduli of quasi-random spatially irregular hexagonal lattices *Int. J. Eng. Sci.* **119** 142–79

[34] Chandra Y, Adhikari S, Mukherjee S and Mukhopadhyay T 2022 Unfolding the mechanical properties of buckypaper composites: nano-to macro-scale coupled atomistic-continuum simulations *Eng. Comput.* **38** 5199–229

[35] Mukhopadhyay T, Naskar S and Adhikari S 2020 Anisotropy tailoring in geometrically isotropic multi-material lattices *Extreme Mech. Lett.* **40** 100934

[36] Singh A, Mukhopadhyay T, Adhikari S and Bhattacharya B 2020 Voltage-dependent modulation of elastic moduli in lattice metamaterials: emergence of a programmable state-transition capability *Int. J. Solids Struct.* **208–209** 31–48

[37] Li K, Gao X-L and Subhash G 2005 Effects of cell shape and cell wall thickness variations on the elastic properties of two-dimensional cellular solids *Int. J. Solids Struct.* **42** 1777–95

[38] Zhu H, Hobdell J and Windle A 2001 Effects of cell irregularity on the elastic properties of 2D voronoi honeycombs *J. Mech. Phys. Solids* **49** 857–70

[39] Zhu H X, Thorpe S M and Windle A H 2006 The effect of cell irregularity on the high strain compression of 2D voronoi honeycombs *Int. J. Solids Struct.* **43** 1061–78

[40] Mukhopadhyay T and Adhikari S 2016 Effective in-plane elastic properties of auxetic honeycombs with spatial irregularity *Mech. Mater.* **95** 204–22

[41] Mizzi L, Attard D, Gatt R, Pozniak A A, Wojciechowski K W and Grima J N 2015 Influence of translational disorder on the mechanical properties of hexachiral honeycomb systems *Composites* B **80** 84–91

[42] Sinha P and Mukhopadhyay T 2022 Effective elastic properties of lattice materials with intrinsic stresses *Thin-Walled Struct.* **173** 108950

[43] Mukhopadhyay T and Kundu D 2022 Mixed-mode multidirectional Poisson's ratio modulation in auxetic 3D lattice metamaterials *Adv. Eng. Mater.* **24** 2101183

[44] Dudek K K, Gatt R and Grima J N 2020 3D composite metamaterial with magnetic inclusions exhibiting negative stiffness and auxetic behaviour *Mater. Des.* **187** 108403

[45] Henderson B, Whitty J, Myler P and Chirwa C 2007 Crash performance of cellular foams with reduced relative density part 2: rib deletion *Int. J. Crashworthiness* **12** 689–98

[46] Pozniak A, Smardzewski J and Wojciechowski K 2013 Computer simulations of auxetic foams in two dimensions *Smart Mater. Struct.* **22** 084009

[47] Zhao R, Kim Y, Chester S A, Sharma P and Zhao X 2018 Mechanics of hard-magnetic soft materials *J. Mech. Phys. Solids* **124** 244–63

[48] Lucarini S, Hossain M and Garcia-Gonzalez D 2021 Recent advances in hard-magnetic soft composites: synthesis, characterisation, computational modelling and applications *Compos. Struct.* **279** 114800

[49] Singh A, Mukhopadhyay T, Adhikari S and Bhattacharya B 2022 Active multi-physical modulation of Poisson's ratios in composite piezoelectric lattices: on-demand sign reversal *Compos. Struct.* **280** 114857

[50] Singh A, Mukhopadhyay T, Adhikari S and Bhattacharya B 2021 Voltage-dependent modulation of elastic moduli in lattice metamaterials: emergence of a programmable state-transition capability *Int. J. Solids Struct.* **208–209** 31–48

[51] Lum G Z, Ye Z, Dong X and Marvi H 2016 Shape-programmable magnetic soft matter *Proc. Natl Acad. Sci.* **41** E6007–15

[52] Hu W, Lum G Z, Mastrangeli M and Sitti M 2018 Small-scale soft-bodied robot with multimodal locomotion *Nature* **554** 81–85

[53] Kim Y, Yuk H, Zhao R, Chester S A and Zhao X 2018 Printing ferromagnetic domains for untethered fast-transforming soft materials *Nature* **558** 274–9

[54] Kim Y, Parada G A, Liu S and Zhao X 2019 Ferromagnetic soft continuum robots *Sci. Robot.* **4** 33

[55] Gonsalez D G and Hossaian M 2021 Microstructural modelling of hard-magnetic soft materials: dipole–dipole interactions versus zeeman effect *Extreme Mech. Lett.* **48** 101382

[56] Furusawa M, Maeda K, Azukizawa S, Shinoda H and Tsumori F 2019 Bio-mimic motion of elastic material dispersed with hard-magnetic particles *J. Photopolym. Sci. Technol.* **32** 309–13

[57] Chen W and Wang L 2020 Theoretical modeling and exact solution for extreme bending deformation of hard-magnetic soft beams *J. Appl. Mech.* **4** 041002

[58] Marckmann G and Verron E 2006 Comparison of hyperelastic models for rubber-like materials *Rubber Chem. Technol.* **79** 835–58

[59] Semler C, Li G X and Paidoussis M P 1994 The non-linear equations of motion of pipes conveying fluid *J. Sound Vib.* **169** 577–99

[60] Chen W and Wang L 2020 Large bending deformation of a cantilevered soft beam under external load: the applicability of inextensibility assumption of the centerline *Curr. Mech. Adv. Mater.* **1** 24–38

[61] Chen W, Yan Z and Wang L 2020 Complex transformations of hard-magnetic soft beams by designing residual magnetic flux density *Soft Matter* **16** 6379–88

[62] Ghuku S and Mukhopadhyay T 2022 Anti-curvature honeycomb lattices for mode-dependent enhancement of nonlinear elastic properties under large deformation *Int. J. Non-Linear Mech.* **140** 103887

[63] Mukhopadhyay T, Adhikari S and Alu A 2019 Probing the frequency-dependent elastic moduli of lattice materials *Acta Mater.* **165** 654–65

[64] Adhikari S, Mukhopadhyay T and Liu X 2021 Broadband dynamic elastic moduli of honeycomb lattice materials: a generalized analytical approach *Mech. Mater.* **157** 103796

[65] Prajwal P, Ghuku S and Mukhopadhyay T 2022 Large-deformation mechanics of anti-curvature lattice materials for mode-dependent enhancement of non-linear shear modulus *Mech. Mater.* **171** 104337

[66] Ding H, Zhen Z, Imtiaz H, Guo W, Zhu H and Liu B 2019 Why are most 2D lattices hexagonal? The stability of 2D lattices predicted by a simple mechanics model *Extreme Mech. Lett.* **32** 100507

[67] Mohamadi Y, Ahmadi H, Razmkhah O and Liaghat G 2021 Axial crushing responses of aluminum honeycomb structures filled with elastomeric polyurethane foam *Thin-Walled Struct.* **164** 107785

[68] Simpson J and Kazancı Z 2020 Crushing investigation of crash boxes filled with honeycomb and re-entrant (auxetic) lattices *Thin-Walled Struct.* **150** 106676

[69] Ghuku S and Mukhopadhyay T 2023 On enhancing mode-dependent failure strength under large deformation: the concept of anti-curvature in honeycomb lattices *Compos. Struct.* **305** 116318

[70] Ngo T D, Kashani A, Imbalzano G, Nguyen K T and Hui D 2018 Additive manufacturing (3D printing): a review of materials, methods, applications and challenges *Composites* B **143** 172–96

[71] Joshi S, Rawat K, Karunakaran C, Rajamohan V, Mathew A T, Koziol K, Thakur V K and Balan A 2020 4D printing of materials for the future: opportunities and challenges *Appl. Mater. Today* **18** 100490

[72] Mitchell A, Lafont U, Hołyńska M and Semprimoschnig C 2018 Additive manufacturing—a review of 4D printing and future applications *Addit. Manuf.* **24** 606–26

[73] Zhou X, Ren L, Song Z, Li G, Zhang J, Li B, Wu Q, Li W, Ren L and Liu Q 2023 Advances in 3D/4D printing of mechanical metamaterials: from manufacturing to applications *Composites* B **254** 110585